THE RAPID INTENSIFICATION OF HURRICANE KARL (2010): NEW REMOTE SENSING OBSERVATIONS OF CONVECTIVE BURSTS FROM THE GLOBAL HAWK PLATFORM

Stephen R. Guimond[1,2], Gerald M. Heymsfield[2], Paul D. Reasor[3], and Anthony C. Didlake, Jr.[2,4]

[1]University of Maryland/Earth System Science Interdisciplinary Center (ESSIC), College Park, Maryland
[2]NASA Goddard Space Flight Center, Greenbelt, Maryland
[3]NOAA Hurricane Research Division, Miami, Florida
[4]Oak Ridge Associated Universities, Oak Ridge, Tennessee

Submitted to the *Journal of the Atmospheric Sciences*

January 14, 2016

Corresponding author address: Stephen R. Guimond, NASA Goddard Space Flight Center, Code 612, Greenbelt, MD 20771.
E-mail: stephen.guimond@nasa.gov

47 **ABSTRACT**
48
49   The evolution of rapidly intensifying Hurricane Karl (2010) is examined from a suite

50   of remote sensing observations during the NASA Genesis and Rapid Intensification

51   Processes (GRIP) field experiment. The novelties of this study are in the analysis of data

52   from the airborne Doppler radar HIWRAP and the new Global Hawk airborne platform

53   that allows long endurance sampling of hurricanes. Supporting data from the HAMSR

54   microwave sounder coincident with HIWRAP and coordinated flights with the NOAA

55   WP-3D aircraft help to provide a comprehensive understanding of the storm. The focus

56   of the analysis is on documenting and understanding the structure, evolution and role of

57   small scale, deep convective forcing in the storm intensification process.

58   Deep convective bursts are sporadically initiated in the downshear quadrants of the

59   storm and rotate into the upshear quadrants for a period of ~ 12 h during the rapid

60   intensification. The aircraft data analysis indicates that the bursts are forming through a

61   combination of two main processes: (1) convergence generated from counter-rotating

62   mesovortex circulations and the larger scale flow and (2) the turbulent transport of warm,

63   buoyant air from the eye to the eyewall at mid-to-low levels. The turbulent mixing across

64   the eyewall interface and forced convective descent adjacent to the bursts assists in

65   carving out the eye of Karl, which leads to an asymmetric enhancement of the warm core.

66   The mesovortices play a key role in the evolution of the features described above.

67   The Global Hawk aircraft allowed an examination of the vortex response and

68   axisymmetrization period in addition to the burst pulsing phase. A pronounced

69   axisymmetric development of the vortex is observed following the pulsing phase that

70   includes a sloped eyewall structure and formation of a clear, wide eye.

1. Introduction

The intensification of tropical cyclones (TCs) is a complex process that is governed by nonlinear coupling of physics across a vast array of space and time scales. On the slow/large scales, a sufficiently warm ocean and low vertical wind shear have been identified as providing favorable environmental conditions for the intensification of TCs (e.g. Kaplan and DeMaria 2003). On the fast/small scales, a large body of evidence has shown that deep, rotating, convective towers are responsible for the intensification, including rapid intensification (RI), of TCs (Steranka et al. 1986; Simpson et al. 1998; Heymsfield et al. 2001; Kelley et al. 2004; Montgomery et al. 2006; Braun et al. 2006; Reasor et al. 2009; Guimond et al. 2010; Molinari and Vollaro 2010; Rogers et al. 2015).

It is the fast/small scales that are the most challenging for the observation, numerical modeling and understanding of TCs. Deep convective towers in TCs have lifetimes of an hour or less with horizontal scales less than 10 km (Montgomery et al. 2006; Houze et al. 2009; Guimond et al. 2010) making it difficult to observe their kinematic properties, especially from conventional aircraft, which can only sample storms for short periods of time (~ 5 h). The turbulent, highly nonlinear character of deep convective towers and their interaction with the TC vortex are major challenges for numerical models and our physical understanding because those scales not explicitly resolved must be parameterized, which are not always adequate (e.g. Persing et al. 2013) and there can be considerable sensitivity to the algorithms used to solve the fluid-flow equations (e.g. Guimond et al. 2016).

The dynamics responsible for the rapid intensification of TCs from localized, deep convection project onto two classes of modes relative to the storm center: axisymmetric

3

95   and asymmetric. In the axisymmetric framework, the projection of localized heat forcing

96   onto the azimuthal mean results in rings of heating typically maximized inside the radius

97   of maximum winds for intensifying storms. Rogers et al. (2013) analyzed a large set of

98   airborne Doppler radar composites of intensifying and steady-state TCs and discovered

99   that a key characteristic of intensifying TCs is the location of deep convective towers

100 inside the radius of maximum winds (RMW). Earlier studies by Schubert and Hack

101 (1982) and Nolan et al. (2007) have elucidated the dynamics of intensifying hurricane

102 vortices finding that convective heating placed inside the RMW enables more efficient

103 conversion of potential to kinetic energy due to the increased inertial stability of the

104 vortex.

105   The heating rings drive an axisymmetric secondary circulation with radial inflow at

106 low levels, updrafts through the core of the heating and radial outflow aloft. In the

107 azimuthal mean, the vortex intensifies through the radial convergence of absolute angular

108 momentum, which is materially conserved above the boundary layer. This framework

109 has been understood for many years (e.g. Shapiro and Willoughby 1982). Other

110 axisymmetric theories for TC intensification have been presented such as the work of

111 Emanuel (1986) and Rotunno and Emanuel (1987), which focus on the cycling of energy

112 extracted through the thermodynamic disequilibrium at the air-ocean interface.

113   In the asymmetric framework, the heating and vorticity asymmetries generated from

114 localized convective forcing interact with the mean flow through eddy heat and

115 momentum fluxes, which can lead to intensification of the vortex for up-gradient

116 transport (Montgomery and Kallenbach 1997). This process is generally called

117 "axisymmetrization" and has been shown to occur in observational (e.g. Reasor et al.

4

118 2000;Reasor et al. 2009) and modeling (e.g. Montgomery et al. 2006;Persing et al. 2013)

119 studies. In nature, the axisymmetric and asymmetric modes are coupled to one another

120 with axisymmetric processes often playing the largest role (e.g. Nolan and Grasso 2003),

121 but with asymmetric dynamics contributing a significant, non-negligible component of

122 the overall system intensification (e.g. Montgomery et al. 2006; Persing et al. 2013;

123 Guimond et al. 2016).

124   In addition to these effects, deep convective towers have also been observed to

125 initiate localized interaction between the eye and eyewall. For example, the studies of

126 Heymsfield et al. (2001) and Guimond et al. (2010), which analyzed very high resolution

127 airborne radar data (along-track sampling of 100 m), showed that deep convective towers

128 intensified the warm core through compensating subsidence around strong updrafts and

129 its turbulent transport towards the eye. This intense, localized transport of air from the

130 eyewall to the eye has important implications for storm intensification through the

131 attendant inward flux of angular momentum.

132   The purpose of this paper is to analyze the rapid intensification (RI) of Hurricane Karl

133 (2010), which coincided with a convective burst episode, from a suite of remote sensing

134 observations to understand more details of the dynamics occurring on the fast/small

135 scales. The novelties of this study are in the use of a new airborne radar and a new

136 airborne platform for hurricane research that allows long endurance (up to 24 h)

137 sampling. Details of these new technologies will be discussed in the next section.

138
139
140 **2. Data and processing**
141
142 *a. HIWRAP*
143

144   The High-Altitude Imaging Wind and Rain Airborne Profiler (HIWRAP) is an

145   airborne Doppler radar that was developed at the NASA Goddard Space Flight Center

146   (GSFC) with the goal of studying hurricanes and other precipitating systems. One of the

147   unique features of HIWRAP is its ability to fly on NASA's Global Hawk (GH)

148   unmanned aircraft, which operates at ~ 18 – 19 km (60 – 62 kft) altitude and can remain

149   airborne for ~ 24 h. The long endurance of the GH is a significant capability for

150   hurricane research. Hurricanes form over remote regions of the ocean with important

151   physical processes occurring on fast time scales that can be easily missed by conventional

152   aircraft that can only remain airborne for ~ 6 h.

153   HIWRAP is a dual-frequency (Ku- and Ka- band), single-polarized (V for inner beam,

154   H for outer beam), downward pointing and conically scanning (16 rpm) Doppler radar

155   with two beams (~ 30° and 40° tilt angles) and 150 m range resolution. The GH aircraft

156   has an airspeed of ~ 160 m s^{-1}, which yields ~ 600 m along-track sampling for HIWRAP.

157   More details on HIWRAP can be found in Li et al. (2015).

158   The NASA Genesis and Rapid Intensification Processes (GRIP) experiment in 2010

159   was the first time HIWRAP collected significant data and some issues with the data

160   quality (e.g. excessive noise at Ku-band due to a variety of issues including pulse

161   processing) were found. To address these issues, we have done two things: (1) pulse pair

162   estimates at Ku-band were reprocessed with 128 pulses averaged (azimuthal resolution of

163   ~ 2.8°), which improves the signal-to-noise ratio (SNR) over the original averaging

164   interval of 64 pulses and (2) Ku-band wind retrievals below the noise saturation level

165   (determined using a power threshold, which translates to ~ 25 dBZ at 3 km height) were

166   replaced with the corresponding Ka-band wind retrievals, which provide a higher SNR

167 and thus, lower uncertainty Doppler velocities in these regions. In the flights over Karl

168 presented in this work, only the inner (30°) beam was functional, which provides a swath

169 width at the surface of ~ 20 – 22 km.

170   Retrievals of the three-dimensional wind vector over the entire radar sampling

171 volume are performed with the three-dimensional variational (3DVAR) algorithm

172 described in Guimond et al. (2014). The 3DVAR method combines an observational error

173 term as well as constraints that include the anelastic mass continuity equation, a

174 Laplacian filter and the impermeability condition at the surface. A coefficient of $2\Delta x^2$

175 was used for the mass continuity constraint and $0.5\Delta x^4$ was used for the filtering

176 constraint with Δx representing the horizontal grid spacing. These values were chosen

177 based on wind vector solution sensitivity tests that provided reasonable accuracy and

178 damping characteristics. The retrievals are performed on a storm-following grid with a

179 horizontal grid spacing of 1 km and vertical spacing of 1 km. Retrievals with vertical

180 spacing of ~ 150 m are possible, but 1 km spacing was deemed sufficient for the present

181 study. NOAA's Hurricane Research Division (HRD), using the Willoughby and

182 Chelmow (1982) method, provided storm center estimates. The mean storm motion

183 vector averaged over the aircraft-sampling period was removed from the HIWRAP

184 derived horizontal winds.

185   Guimond et al. (2014) showed that simulated and *in situ* errors for the horizontal

186 wind components were ~ 2.0 m s^{-1} or ~ 7 % of the hurricane wind speed. The errors in

187 the vertical velocity were strongly dependent on the across-track location of the

188 measurements with comparisons to *in situ* data revealing errors of ~ 2.0 m/s at nadir.

189 These *in situ* errors used data from the Imaging Wind and Rain Airborne Profiler

190 (IWRAP) flying on the NOAA P3 aircraft, which has a similar scanning geometry to

191 HIWRAP. The appendix presents comparisons of *in situ* data to HIWRAP retrievals,

192 which reveal that for wind speeds > 10 m s^{-1} the mean error in the computed wind speed

193 and direction is $\sim 1 - 4$ m s^{-1} and $\sim 10 - 20°$, respectively.

194 *b. NOAA P3 Radars*

195   The NOAA P3 tail (TA) radar is an X-band airborne Doppler radar that scans in a

196 cone 20° fore and aft of the plane perpendicular to the aircraft with a scan rate of 10 rpm

197 and along-track sampling of fore/aft sweeps of ~ 1.6 km (Gamache et al. 1995).

198 Retrievals of the three-dimensional wind vector are performed using the variational

199 methodology outlined in Gamache (1997) and Reasor et al. (2009) at a grid spacing of 2

200 km in the horizontal and 0.5 km in the vertical. Quality control procedures on the raw

201 observations of reflectivity and radial velocity can be found in Gamache et al. (2005).

202 The mean storm motion vector averaged over the aircraft-sampling period was removed

203 from the TA derived horizontal winds.

204   The NOAA P3 aircraft also carries a C-band Lower Fuselage (LF) radar that provides

205 a scan of radar reflectivity every 30 seconds at approximately the flight-level height.

206 This data is useful for identifying and tracking vortex and convective scale features of

207 TCs close to the aircraft. The large vertical beamwidth of 4.1° can cause smearing of

208 features and inadequate beam filling for ranges greater than ~ 60 km (Marks 1985).

209 Analysis of the LF data is confined to ranges less than 50 km to avoid these problems.

210 *c. HAMSR*

211   The High-Altitude Mimic Sounding Radiometer (HAMSR) is a passive microwave

212 sounder measuring upwelling radiation from the atmosphere at frequencies sensitive to

8

213   temperature (~ 50 GHz and ~ 118 GHz) and water vapor (~ 183 GHz). The intensity of

214   convective clouds can also be estimated in regions where upwelling radiation is scattered

215   out of the beam by ice particles, which results in anomalously low brightness

216   temperatures (Tbs) at the instrument receiver. The HAMSR instrument scans +/- 60°

217   across-track providing a swath width of ~ 65 km from the height of the GH aircraft.

218   However, we focus on data at +/- 45° because larger errors are found beyond this range

219   (Brown et al. 2011). The footprint of HAMSR at nadir from the GH altitude is ~ 2 km

220   with an increase in size as the instrument scans off-nadir. The along-track sampling of

221   HAMSR measurements is ~ 250 m. In this study, the HAMSR Tbs are mapped to a grid

222   with 1 km spacing to match the HIWRAP wind retrievals. The vertical resolution of the

223   HAMSR data is dictated by each channel's weighting function, which amounts to ~ 2 – 3

224   km intervals in height. More detailed information on HAMSR can be found in Brown et

225   al. (2011).

226
227   **3. Overview of Hurricane Karl**
228
229   During the summer of 2010, NASA conducted the GRIP field experiment in the

230   Atlantic Ocean basin to study the physical processes controlling hurricane formation and

231   intensity change. A total of three NASA aircraft were deployed during GRIP with

232   instruments onboard to measure properties of the hurricane environment and inner-core

233   region. In this study, we focus on the inner-core aircraft (GH) and instruments

234   (HIWRAP and HAMSR) described in the previous section. Further information about

235   GRIP can be found in Braun et al. (2013).

236   Hurricane Karl began from a combination of a tropical wave moving off the African

237   coast and an elongated trough of low pressure situated over the southwestern North

238   Atlantic Ocean. Figure 1 shows the best track of Karl and intensity classifications

239   starting at 0000 UTC 14 September. Over several days time, deep convection located

240   near the wave axis became more organized and by 1200 UTC 14 September a tropical

241   depression formed in the northwestern Caribbean Sea (Stewart 2010). Not long after,

242   Karl intensified to a tropical storm and made landfall on 15 September on the Yucatan

243   Peninsula with surface winds of ~ 27 m s^{-1}. Karl weakened while crossing land, but was

244   able to maintain tropical storm classification (~ 20 m s^{-1} surface winds) with a well-

245   organized circulation.

246   After emerging into the Bay of Campeche, Karl rapidly intensified from a ~ 20 m s^{-1}

247   tropical storm on 0600 UTC 16 September to a ~ 57 m s^{-1} hurricane on 1200 UTC 17

248   September (Fig. 1). This equates to a ~ 37 m s^{-1} increase in surface winds in a 30 h

249   period, which is more than double the typical RI rate of ~ 15 m s^{-1} in 24 h (Stewart 2010).

250   Our focus in this study is the inner-core structure and dynamics during this RI episode

251   that was sampled by the GH aircraft between ~ 1900 UTC 16 September and ~ 0800

252   UTC 17 September (see Fig. 1).

253   From an environmental perspective, Karl was primed for RI with high sea-surface

254   temperatures of ~ 30° C in the Bay of Campeche, relatively low vertical wind shear of ~

255   5 m s^{-1} with the vector pointing mostly towards the southwest over the RI interval, and

256   moist mid-level air. The large-scale vertical wind shear impacting the storm was

257   determined from CIMSS satellite analyses and verified using NCEP re-analysis data.

258

259   **4. Convective burst remote sensing observations**

260   *a. Satellite evolution*

261   Animations of GOES IR satellite data indicate that localized convective bursts in Karl

262   were actively pulsing for a ~ 12 h period between 1200 UTC 16 September and 0000

263   UTC 17 September. After this time period, the convective forcing is less frequent and a

264   more axisymmetric presentation of the cloud field emerges.

265   Figure 2 shows a sequence of GOES IR images of Karl spanning the period of GH

266   observations during the storm's RI. The GOES IR data has a resolution of ~ 4 km. On

267   1845 UTC 16 September (Fig. 2a), a region of asymmetric cold cloud tops (~ -80° C)

268   associated with a pulsing convective burst is located in the downshear to downshear-left

269   portions of the storm. No apparent eye is visible at this time due to the presence of heavy

270   cloud. At 2215 UTC (Fig. 2b), the convective burst episode is still evident in the IR

271   imagery with deep convection located in the downshear-left sector of the storm and the

272   appearance of a cloud filled eye. A few hours later at 0140 UTC 17 September (Fig. 2c),

273   the cold cloud top region has wrapped around to the upshear quadrants of the storm. A

274   clearer depiction of an eye is present at this time although it is still not cloud free.

275   Towards the end of the aircraft observation period at 0501 UTC (Fig. 2d), the cold cloud

276   tops have diminished and spread around the storm in a more axisymmetric pattern along

277   with the development of a large, clear eye. Karl is nearing landfall at this point, but the

278   core region of the storm is still well offshore.

279   The satellite presentation of Karl's RI with localized convective bursts pulsing in the

280   downshear quadrants of the storm, their rotation and dissipation into the upshear

281   quadrants and development of an axisymmetric cloud structure with a clear eye at late

282   times is common (e.g. Reasor et al. 2009; Guimond et al. 2010; Stevenson et al. 2014).

283   In addition, the presence of lightning associated with convective bursts has become more

11

284 commonly recognized. Rinehart et al. (2014) analyzed satellite data and several GRIP

285 datasets and found that some of the more intense convective burst activity in Karl

286 produced significant lightning.

287 *b. HIWRAP time-averaged structure*

288   The spatial and temporal evolution of convective bursts is very turbulent in nature

289 and requires high-resolution aircraft measurements to accurately describe their structure.

290 A time-averaged view of the storm from HIWRAP radar measurements is first presented

291 and then individual overpasses are analyzed from several data sources to highlight the

292 detailed structure of convective bursts during the pulsing phase. Finally, we briefly show

293 the structure of the vortex during the axisymmetric response phase.

294   Figure 3a shows HIWRAP Ku-band reflectivity overlaid with horizontal wind vectors

295 at 2 km height on a storm-relative grid averaged over the entire GH sampling interval (~

296 1900 UTC 16 September - 0800 UTC 17 September). A broad cyclonic circulation is

297 evident with a reflectivity filled eye, which is weighted towards early time periods.

298 There are gaps in the azimuthal coverage of the storm due to the small swath width of

299 HIWRAP. These gaps decrease towards the storm center where estimates of the low

300 wavenumber components of the flow are best suited.

301   Figure 3b shows the horizontal wind speeds at 2 km height averaged over the same

302 time interval. The strongest winds are generally located in the downshear quadrants of

303 the storm with large patches of $\sim 40 - 45$ m s^{-1} winds in this region. The time and

304 azimuthally averaged RMW at this level is $20 - 25$ km. An interesting feature appearing

305 in the data is the presence of small clusters of anomalously large wind speeds in the

306 eyewall (two examples are labeled with white arrows in Fig. 3b). These clusters have a

307   length scale of ~ 10 km and are found most notably in the downshear direction and

308   downshear-left quadrant just inside the RMW.

309   Figure 4a is similar to Fig. 3a only at 8 km height centered on the inner 50 km of the

310   storm. At this higher level, the presence of convective bursts shown by the high

311   reflectivity anomalies between ~ 25 – 40 dBZ are evident. These bursts are occurring in

312   the downshear to downshear-left portions of the storm with evidence of rotation into the

313   upshear quadrants. This structure is consistent with the satellite data shown in Fig. 2,

314   only the HIWRAP data is much higher resolution and individual convective elements are

315   discernable. The majority of the burst activity over this time interval is located inside the

316   low-level (2 km) RMW, which is consistent with the intensifying TC composite of

317   Rogers et al. (2013). The patches of anomalously large wind speeds shown in Fig. 3b are

318   well correlated with the high reflectivity anomalies in Fig. 4a, which *suggests the*

319   *connection of the convective bursts to the localized spin-up of the low-level wind field.*

320   The association of the high reflectivity anomalies aloft to the localized low-level wind

321   spin-up is burdened by the 12 – 13 h time-averaged perspective. However, individual

322   overpasses were analyzed and they confirmed the existence of this relationship.

323   Figure 4b shows the horizontal wind speeds at 8 km height, which reveals similar

324   cellular structures as the 2 km wind speeds albeit with generally reduced magnitudes. The

325   strongest wind speeds of ~ 35 – 40 m s^{-1} are found in the downshear-left quadrant and the

326   northeast, upshear quadrant at 8 km height. This shows that the enhanced winds

327   associated with the convective bursts extend through a deep layer with the downshear-left

328   quadrant containing the most intense winds.

329   *c. Airborne radar and radiometer analysis during the burst pulsing phase*

330   1) 1ST SAMPLING PERIOD (~ 1830 – 1920 UTC 16 SEPTEMBER)

331   The NOAA P3 aircraft sampled the RI of Karl at certain similar time periods as the

332   NASA GH, which allows a more comprehensive study of the inner-core processes due to

333   the large swath width of the P3 measurements. The P3 first crossed the storm center at ~

334   1842 UTC 16 September. The LF radar reflectivity at flight level (3.7 km height) along

335   with the TA radar derived wind vectors are shown in Fig. 5a at this time.

336   An interesting wavenumber-5 polygon structure is apparent at the eye/eyewall

337   interface in the LF reflectivity, which is indicative of the presence of mesovortices at the

338   locations of the vertices. The study of Hendricks et al. (2012) observed similar

339   reflectivity structures in the rapid intensification of Hurricane Dolly (2008). The

340   formation of mesovortices has been linked to dynamic instability in the eyewall where

341   thin rings of potential vorticity support the phase locking and exponential growth of

342   counter-propagating vortex Rossby waves (e.g. Schubert et al. 1999; Kossin and Schubert

343   2001; Rozoff et al. 2009; Hendricks et al. 2014). The above studies showed that

344   development of mesovortices is an effective means of turbulent mixing between the eye

345   and eyewall, which can lead to important consequences for the intensity of the hurricane.

346   The wind vectors in Fig. 5a show that the strongest winds (~ 40 m s^{-1}) are located in

347   the upshear (northeast) quadrant at this time and level (4 km height), which is more

348   consistent with the time-averaged HIWRAP data at 8 km height (Fig. 4b) than at 2 km

349   height (Fig. 3b). Figure 5b highlights the 1 – 4 km mean radial component of the flow

350   for this transect along with perturbation wind vectors (computed by removing the

351   azimuthal mean radial and tangential winds from the total flow and projecting back to

352   Cartesian space) averaged over the same height interval. The analysis in Fig. 5b shows a

14

353   significant region of outflow emerging from the eye and entering the southern eyewall

354   (see thick arrow in Fig. 5b) where an intense band of ~ 40 dBZ echoes are observed (Fig.

355   5a). The outflow from the eye likely brings warm anomaly air into the eyewall, which

356   helps to stimulate convection through buoyancy effects.

357   A broad region of inflow located radially outside the outflow feature (see thin arrow

358   in southern half of Fig. 5b) enables kinematic convergence to help develop and sustain

359   the intense convection in the southern eyewall as well. This convergence signature is

360   vertically coherent down to 1 km height, which was validated by computing the

361   divergence field (not shown). In the northwestern portion of the eyewall, a wide inflow

362   region (see thick arrow in Fig. 5b) with peak magnitudes of ~ -8 m s^{-1} is transporting air

363   across the eye-eyewall interface. The perturbation wind vectors show that a

364   cyclonic/anti-cyclonic mesovortex couplet is responsible for the transport of air across

365   the eye-eyewall interface on the northwestern side extending down across the southern

366   side.

367   Figure 6a shows HAMSR 54 GHz Tbs overlaid with HIWRAP computed horizontal

368   wind vectors from the first GH overpass of Karl between 1853 – 1919 UTC 16

369   September. The aircraft crossed the storm center at ~ 1910 UTC, which is ~25 minutes

370   after the P3 transect shown in Fig. 5. The data is shown at 2 km height, which is where

371   the HAMSR 54 GHz weighting function peaks, assuming a standard atmosphere. The

372   presence of light precipitation in the eye of Karl at this time allows the flow in the eye

373   and its interaction with the eyewall to be analyzed.

374   In this pass, the warm anomaly of Karl is evident shown by the anomalously large

375   Tbs in the core of the storm. For this analysis we are not as interested in the quantitative

376   properties of the warm core as our focus is on the qualitative structure of this feature.

377   The eyewall of Karl with embedded convective bursts is seen by the depressed Tbs in the

378   southern half of Fig. 6a with an intense cell located in the eastern half of the southern

379   eyewall, which is in the downshear-left quadrant. The azimuthal mean RMW at this time

380   and height is ~ 30 km, which places the cell inside the RMW. The winds in this region

381   are 30 – 40 m s^{-1} as computed from HIWRAP data.

382   An interesting feature of the HAMSR data is a finger-like protrusion of the warm core

383   sticking out of the southern eyewall and adjacent to the most intense convective activity

384   (labeled with white arrows in Fig. 6a). The HIWRAP winds follow this feature well and

385   show 10 – 20 m s^{-1} flow originating in the eye and cyclonically rotating towards the

386   intense convective cell in the eastern half of the southern eyewall. The winds from this

387   warm anomaly protrusion show a convergence signature with the intense convective cell.

388   Figure 6b shows Ku band reflectivity from HIWRAP along with horizontal wind

389   vectors for the same overpass as in Fig. 6a. The warm core protrusion observed in the

390   HAMSR data can also be seen in the HIWRAP data through reduced reflectivity in the

391   southern eyewall from values of 35 – 40 dBZ to ~ 20 dBZ. *It appears that turbulent*

392   *mixing between the warm, dry air in the eye with the eyewall is helping to carve out and*

393   *develop the eye of Karl.* In addition to the HIWRAP winds in Fig. 6, the LF reflectivity

394   structure (Fig. 5a) and TA perturbation winds (Fig. 5b) observed ~ 25 minutes earlier

395   show that the turbulent mixing is a result of mesovortices located near the eye/eyewall

396   interface. Small patches of reduced reflectivity (Fig. 6b) in the same locations as the low

397   TBs in Fig. 6a are the result of attenuation of the HIWRAP Ku band signal from the

398   convective bursts.

16

399   Figure 7 shows nadir cross-sections of HIWRAP data for the first GH overpass (see

400   Fig. 6). This cross-section is straight through the storm center in the north-to-south

401   direction. Figure 7a shows Ku band reflectivity through the convective burst in the

402   southern eyewall revealing a deep column of high values reaching ~ 35 dBZ at 12 km

403   height (x-axis ~ -25 km). There is a large region of lower reflectivity (~ 20 dBZ) filling

404   the eye that appears connected with the convective burst in the southern eyewall. In the

405   eye region, there is a deep layer (1 – 10 km) of outflow with magnitudes of ~ 10 – 15 m s^{-}

406   ^{1} (Fig. 7b, x-axis ~ -15 km), which is consistent with the warm core mixing into the

407   eyewall shown in Fig. 6a at 2 km height. The outflow from the eye converges with

408   inflowing air, located radially outside the convection, at low-to-mid levels in the core of

409   the burst (see gray arrows in Fig. 7b). *This data indicates that the formation/maintenance*

410   *of the convective burst in the southern eyewall (downshear-left quadrant) is driven by a*

411   *combination of buoyancy (inferred from Fig. 6a) and horizontal, kinematic convergence*

412   *(Fig. 7b). Both of these mechanisms are facilitated by the turbulent mixing of air,*

413   *originating in the anomalously warm eye, with inflowing air in the low-to-mid level*

414   *eyewall.* In the northern part of the eyewall in Fig. 7b, the radial flow reflects traditional

415   azimuthal mean behavior with inflow at low levels and outflow aloft.

416   A significant region of descent with peak values of ~ -3 m s^{-1} is located in the eye of

417   Karl (wide gray arrow in Fig. 7c), which should be helping to clear and warm the eye.

418   This descent appears to be induced by the convective updraft (thin gray arrow in Fig. 7c)

419   occurring on the inner edge of the eyewall (x-axis ~ -15 km). A reasonably strong

420   updraft of ~ 10 m s^{-1} (Fig. 7c) in the core of the deep convection (x-axis ~ -25 km) is

421   coincident with an anomalously large patch of cyclonic vorticity (Fig. 7d) at ~ 7 km

17

422 height. Note that vorticity values are removed above 10 km height because the swath

423 width of the HIWRAP data at these levels is very small, which places the swath edges

424 close to nadir. The computed horizontal winds at the swath edges have larger uncertainty

425 due to the HIWRAP scanning geometry (Guimond et al. 2014). At low levels on the

426 inner edge of the deep convection (x-axis ~ -18 km), a weak-moderate updraft (Fig. 7c) is

427 collocated with an intense cyclonic vorticity anomaly with values of 10^{-2} s^{-1} (Fig. 7d).

428   These observations suggest that the convective burst sampled here is rapidly rotating

429 through a deep layer as has been observed in previous studies (e.g. Reasor et al. 2005;

430 Houze et al. 2009). For a mature TC such as Karl, the production of vorticity is likely

431 dominated by the stretching of pre-existing cyclonic vorticity in the eyewall (e.g.

432 Montgomery et al. 2006). In the northern portion of the eyewall, an elevated band of

433 cyclonic vorticity that tilts outward with height is observed (Fig. 7d), which fits more

434 closely with typical azimuthal mean TC structure.

435   2) 2nd SAMPLING PERIOD (~ 1920 – 2000 UTC 16 SEPTEMBER)

436   Approximately 20 minutes after the first GH overpass, the NOAA P3 aircraft

437 penetrated the core of Karl again with a center crossing at ~ 1930 UTC 16 September.

438 Figure 8a shows LF radar reflectivity at flight level (3.6 km height) along with the TA

439 radar derived wind vectors at 4 km height. Intense reflectivity between 45 – 50 dBZ is

440 present on the western half of the storm while the eastern half is ragged without a

441 continuous region of elevated reflectivity. Significant reflectivity is located in the eye of

442 the storm and animations of several LF scans show mesovortex-like features mixing into

443 the eye from the eyewall. Much like the previous transect, the strongest winds are

444 located in the northeast (upshear) quadrant.

445   Figure 8b shows the perturbation wind vectors, averaged over the 1 – 4 km height

446   interval, overlaid on the mean divergence field in this same layer. A wavenumber-2

447   divergence pattern is observed with strong regions of convergence in the western and

448   eastern portions of the eyewall. The convergence region in the western eyewall

449   (downshear quadrants) is consistent with the intense reflectivity band (Fig. 8a), while the

450   eastern eyewall (upshear quadrants) is having difficulty developing perhaps as a result of

451   the vertical wind shear. The perturbation wind vectors reveal a similar cyclonic/anti-

452   cyclonic mesovortex couplet as the previous transect (Fig. 5b) although a data gap in the

453   southwestern quadrant in Fig. 8b makes the placement of the anti-cyclonic circulation

454   rather broad and with some uncertainty. The counter-rotating circulations are consistent

455   with the divergence signatures and are directing air across the eye-eyewall interface with

456   inflow to the eye on the western side and outflow to the eyewall on the eastern side.

457   Figure 9 is similar to Fig. 6a only for the second GH overpass of Karl between 1938 –

458   1957 UTC 16 September. This is a diagonal pass from southeast to northwest, which

459   covers part of the upshear left quadrant of the storm where depressed Tbs from HAMSR

460   show the straining/elongation of deep convection by the advective tendencies of the

461   cyclonic flow. The maximum HIWRAP winds at 2 km height are ~ 50 m s^{-1} in the

462   northwest eyewall and ~ 30 m s^{-1} in the southeast eyewall where the flow has a radially

463   outward directed component into the convection. The warmest Tbs are located on the

464   northwestern side of the eye.

465   The vertical structure of HIWRAP Ku band reflectivity at nadir for this overpass is

466   shown in Fig. 10a. Deep convection with similar vertical structure and radial location to

467   that shown in the previous GH overpass (Fig. 7a) is observed in the southeastern (upshear

19

468   left) portion of the eyewall with significant reflectivity filling the eye adjacent to this cell.

469   The northwest portion of the eyewall is not as convectively active and the eye is clear

470   adjacent to this side of the eyewall, which is consistent with the previous overpass and

471   the warmest Tbs shown in Fig. 9.

472   Figure 10b shows the radial wind speeds for this overpass. The dominant features are

473   a region of midlevel inflow located radially outside the convective burst and a deep

474   column of strong outflow that traverses the eye region and enters the core of the burst

475   (see gray arrows). These winds acquire entropy from the warm anomaly eye (see Fig. 9)

476   likely leading to assistance in convective development in the southeastern eyewall

477   through buoyancy effects. The flow across the eye is similar to that observed by the P3

478   shown in Fig. 8b and is driven by the counter-rotating mesovortex circulations. On the

479   northwestern side of the storm, low-level inflow and mid-level outflow resembles

480   azimuthal mean hurricane structure.

481   The vertical motion structure in Fig. 10c shows a broad region of descent in the eye

482   adjacent to the convective burst with values of $\sim$ -2 $-$ -4 m s^{-1}. This descent appears to be

483   generated by the convective activity through compensating motions around convective

484   updrafts (see gray arrows). The broad region of forced descent in the eye is similar to

485   that observed in the previous overpass in the downshear-left quadrant. This robust

486   structure should lead to a drying and warming effect over time, which will be

487   demonstrated with the data in subsequent overpasses.

488   Finally, instead of showing the vorticity for this overpass, which was somewhat

489   similar to the previous transect, the tangential winds are presented in Fig. 10d. The

490   tangential winds are $\sim$ 20 m s^{-1} stronger in the northwest eyewall up to midlevel regions

491   with peak values of ~ 50 m s^{-1} at low levels. In the deep convection, large tangential

492   wind speeds are located at high levels (12 – 13 km), which is due to strong updrafts

493   transporting high angular momentum air aloft. It appears the convective towers are

494   trying to build a deeper, more intense vortex in this portion of the eyewall.

495   3) 3rd SAMPLING PERIOD (~ 2030 – 2100 UTC 16 SEPTEMBER)

496   The NOAA P3 tracked through the center of Karl one last time centered at 2042 UTC

497   16 September. Figure 11a shows the LF reflectivity at flight level (3.6 km) along with

498   TA derived wind vectors at 4 km height for this transect. The western eyewall continues

499   to be the dominant feature with a large region of reflectivity at or above 50 dBZ. An

500   animation of several LF scans within ± 2 minutes of the one shown in Fig. 11a indicates

501   that the western eyewall with embedded deep convective towers is intensifying rapidly

502   (in terms of reflectivity) during the P3 penetration of the core. The horizontal winds in

503   this region are ~ 10 m s^{-1} stronger than those from the previous P3 sampling ~ 1 hour

504   earlier at 1930 UTC (see Fig. 8a). The eastern eyewall is still ragged without a coherent

505   eyewall apparent in the reflectivity, while the southern eyewall has increased banding

506   features, which appear to be coalescing.

507   The divergence field for this flight averaged over the 1 – 4 km layer is shown in Fig.

508   11b with 1 – 4 km height averaged perturbation winds overlaid. The cyclonic/anti-

509   cyclonic mesovortex couplet identified in the previous P3 penetrations continues to

510   persist two hours after initial diagnosis. At this time period, the mesovortex couplet has

511   rotated cyclonically with the mean flow placing the cyclonic circulation directly North of

512   the anti-cyclonic circulation in the western eyewall. These circulations are consistent

513   with a strong region of convergence in the western eyewall, which is helping to develop

21

514   the convective bursts, and a west-to-east flow across the eye. In the eastern eyewall,

515   which is not well defined in the LF reflectivity, another small-scale cyclonic circulation is

516   evident in the perturbation wind vectors. This circulation is helping to direct a southerly

517   flow across portions of the eastern eye-eyewall interface.

518   The next GH overpass of Karl sampled directly along the shear vector with a

519   southwest to northeast transect just north of the storm center at ~ 2040 UTC 16

520   September, which is ~ 2 minutes behind the P3. Figure 12 shows HAMSR 54 GHz Tbs

521   along with HIWRAP horizontal wind vectors at 2 km height for this overpass. A very

522   intense convective cell located in the down-shear direction is present in the HAMSR data

523   with Tbs falling well below 200 K (strong ice scattering) in the core of the ~ 10 km wide

524   feature. This cell is located at and just inside the azimuthally averaged RMW at this

525   level.

526   In the eye of the storm, the HIWRAP winds reveal a cyclonic mesovortex circulation

527   that is directing air out of the northern portion of the eye and into the convective burst.

528   The HAMSR data shows that the air being transported into the burst is anomalously

529   warm with Tbs significantly larger than ambient values. The mesovortex circulation

530   identified in the HIWRAP data is also seen at the same location in the TA perturbation

531   wind vectors (see Fig. 11b).

532   The close coordination of the GH and P3 aircraft during this time allows a

533   comparison of the storm structure from the HIWRAP and TA radars. The appendix also

534   shows error statistics between HIWRAP computed winds and P3 flight level data. Figure

535   13a shows HIWRAP Ku band reflectivity in a vertical cross section averaged between ~

536    $0 - 6$ km in the +y direction (see Fig. 12 for averaging domain) while Fig. 13b shows the

537   same field only for the TA X band data. Both radars show similar qualitative structures

538   with a deep convective cell and elevated reflectivity to ~ 15 km height in the downshear

539   eyewall of Karl. However, the quantitative structure of this cell differs to some extent

540   with HIWRAP revealing a more intense, concentrated reflectivity signature while the P3

541   TA radar shows a weaker and more diffuse cell.

542   These differences are due to several things: the higher resolution (sampling) of the

543   HIWRAP radar, the use of a Gaussian distance-weighted interpolation in the TA data,

544   calibration biases with both radars and rapid evolution of the convection over the ~ 2

545   minute sampling offset. The smoothing in the interpolation used to produce the gridded

546   TA data plays a significant role in the reflectivity differences. A higher resolution TA

547   product that minimizes smoothing was also analyzed and showed increases in reflectivity

548   magnitudes of ~ 5 – 10 dBZ (not shown), which are more similar to HIWRAP.

549   Unfortunately, this product is only available in a vertical slice along the aircraft track,

550   which prevents the presentation of the mean structure of the inner core shown in Fig. 13

551   and subsequent figures. Therefore, we proceed with the default TA dataset.

552   The radial winds from HIWRAP (Fig. 14a) show a strong convergence signature

553   (divergence field was computed, but not shown) directly below the intense convective

554   cell with outflow of ~ 5 – 8 m s^{-1} crossing the eye-eyewall interface. This outflow from

555   the eye brings warm anomaly air into the eyewall helping to fuel the convective cell as

556   was shown in Fig. 12. The TA radar radial winds (Fig. 14b) show similar features in

557   similar locations, but the intensity of the flow is reduced. The higher resolution TA

558   product agrees more closely with HIWRAP.

559   A deep column (1 – 12 km) of inflow ($\sim$ -5 – -10 m s^{-1}) coincident with the

560   convective cell is present in the HIWRAP data (Fig. 14a) and in the TA data at low and

561   high levels (Fig. 14b), which acts to locally spin-up the tangential winds through the

562   inward transport of high angular momentum air. The proximity of the cell to the center

563   of circulation (inside RMW of $\sim$ 23 km) also allows strong projection onto the azimuthal

564   mean dynamics.

565   Figure 15a shows the HIWRAP derived vertical winds in the downshear eyewall for

566   this same averaged section of data. A deep updraft is present in the core of the

567   convective cell with a strong pulse approaching 10 m s^{-1} located above 10 km height. A

568   downdraft of $\sim$ -3 m s^{-1} is located on the inner edge of the eyewall (see gray arrow),

569   which is likely formed through mass conserving motions around the strong updraft. The

570   TA vertical winds in Fig. 15b show similar structure to that from HIWRAP with a deep,

571   wide updraft maximized at $\sim$ 10 km height, but again with reduced magnitudes. The TA

572   data also shows compensating downdrafts on either side of the updraft with a broad

573   region of descent ($\sim$ -1 – -2 m s^{-1}) located radially inward of the cell (see gray arrow).

574   This broad descent is well positioned to dry and warm the eye as observed in previous

575   overpasses (see Fig. 7c and Fig. 10c). This is also true of the HIWRAP observed inner-

576   edge downdraft and is a common feature around convective towers located in the eyewall

577   of intensifying TCs (e.g. Heymsfield et al. 2001; Guimond et al. 2010).

578   *d. HIWRAP data analysis during the vortex response phase*

579   The main advantage of the GH aircraft is the long duration sampling, which allows

580   continued analysis of the RI of Karl when the P3 aircraft returned to base following the

581   2042 UTC 16 September eye penetration. The GOES IR satellite data analyzed in

24

582   section 4a showed that the majority of the convective burst activity was finished by ~

583   0000 UTC 17 September. After this time, the vortex went through a response phase that

584   included axisymmetrization of the convective anomalies, which was sampled by the GH

585   aircraft for a period of ~ 8 h.

586   Figure 16 shows vertical cross sections of HIWRAP Ku band reflectivity and

587   tangential wind speed at nadir for a series of overpasses of the inner-core of Karl

588   spanning this 8 h period. At 0012 UTC 17 September (Fig. 16a), the vertical structure of

589   the eye/eyewall already looks different than that shown for the burst pulsing phase (e.g.

590   Fig. 7a and Fig. 10a). There is little reflectivity filling the eye, and the beginning of a

591   more sloped structure to the eyewall is observed. The tangential winds peak at ~ 40 m s^{-1}

592   in the southeast quadrant and ~ 45 m s^{-1} in the northwest quadrant with both sides

593   showing contours sloping outward with height. About 3.5 h later at 0345 UTC (Fig.

594   16b), the axisymmetric structure reflected in the cross-section continues to develop with

595   significant sloping of the eyewall reflectivity and tangential winds with height. The eye

596   has also widened, which is indicative of increased subsidence and growth of the warm

597   core (backed by HAMSR data; not shown) in association with an enhanced secondary

598   circulation from the vortex response to the convective forcing.

599   Over the next ~ 4 h, the trend towards a wider, clearer and warmer eye with a sloping

600   eyewall structure reminiscent of axisymmetric hurricanes continues to prevail (Figs. 16c

601   and 16d), except for the presence of a transient convective burst in the northwest eyewall

602   in Fig. 16c.

603

604   **5. Conclusions**

605   In this paper, the evolution of rapidly intensifying Hurricane Karl (2010) is examined

606   from a suite of remote sensing observations during the NASA Genesis and Rapid

607   Intensification (GRIP) field experiment. The novelties of this study are in the analysis of

608   data from a new airborne Doppler radar (HIWRAP) and a new airborne platform (NASA

609   Global Hawk) for hurricane research that allows long endurance sampling (up to 24 h).

610   Supporting data from a microwave sounder (HAMSR) coincident with HIWRAP and

611   coordinated flights with the NOAA WP-3D aircraft carrying the lower fuselage (LF) and

612   Tail (TA) radars help to provide a detailed analysis of the storm. The focus of the

613   analysis is on documenting and understanding the structure, evolution and role of small

614   scale, deep convective forcing in the storm intensification process.

615   After Karl emerged off the Yucatan Peninsula as a tropical storm, satellite data

616   revealed the presence of deep convective bursts located primarily in the downshear to

617   downshear-left quadrants of the storm. The bursts went through a ~ 12 h pulsing phase

618   followed by a vortex response phase that included axisymmetrization of the convective

619   anomalies and the development of a wide, clear eye. During the time period of the burst

620   pulsing and vortex response phase, the surface wind speeds in Karl increased by ~ 37 m

621   s^{-1} in a 30 h period, which is more than double the typical rapid intensification rate of ~

622   15 m s^{-1} in 24 h (Stewart 2010).

623   The Global Hawk (GH) and P3 aircraft data was analyzed from ~ 1900 UTC 16

624   September – 0800 UTC 17 September, which covered portions of the convective burst

625   pulsing phase and vortex response phase. The aircraft remote sensing data and analysis

626   indicates the following science results.

627   The convective bursts formed primarily in the downshear to downshear-left quadrants

628   through a combination of two main processes: (1) convergence generated from counter-

629   rotating mesovortex circulations and the larger scale flow and (2) the turbulent transport

630   of warm, buoyant air from the eye to the eyewall at low-to-mid levels. Reflectivity

631   snapshots and animations from the LF radar showed a distinct wavenumber-5 structure at

632   the eye/eyewall interface and movement of small-scale features in the eye and across the

633   interface during the aircraft-sampling period. These structures and the observed turbulent

634   mesovortex circulations that produce significant eye-eyewall mixing form as a result of

635   dynamic instability in the axisymmetric vortex (e.g. Schubert et al. 1999; Kossin and

636   Schubert 2001; Rozoff et al. 2009; Hendricks et al. 2012).

637   Horizontal wind fields computed from the TA and HIWRAP measurements showed

638   that the mesovortex circulations were primarily located in the western and southern

639   (downshear) eye/eyewall region where the most intense convective activity was found.

640   In one GH overpass, a finger-like protrusion of the warm core observed from HAMSR

641   was observed to rotate cyclonically into the eyewall, likely helping to fuel convective

642   towers observed in this region. The array of mesoscale circulations and convective bursts

643   rotated cyclonically with the mean flow over time. As the bursts rotated into the upshear

644   quadrants, they were influenced by an across eye flow induced by the counter-rotating

645   mesovortex circulations. Figure 17 shows a conceptual diagram summarizing the remote

646   sensing measurements and the analysis of the mesoscale dynamics described above.

647   The mechanism for convective burst formation identified in the observations is

648   similar to that determined by Braun et al. (2006) using a numerical simulation of

649   Hurricane Bonnie (1998). In this study, the initiation of updraft towers was found to

27

650   result from convergence between shear induced asymmetries and the cyclonic flow

651   associated with eyewall mesovortices. Reasor et al. (2009) also found observational

652   evidence for the triggering of convective bursts through the interaction of low-level

653   environmental flow and low-wavenumber vorticity asymmetries in the eyewall of

654   Hurricane Guillermo (1997). The HIWRAP and P3 TA radar analysis described in this

655   paper highlights a similar convergence mechanism with the addition of significant

656   transport of warm, buoyant air from the eye into the eyewall as indicated by the

657   HIWRAP and HAMSR data. This additional piece of evidence linked to the formation

658   and/or maintenance of the convective bursts is supported by the trajectory analysis of a

659   numerically simulated hurricane by Cram et al. (2007).

660   The formation of a clear eye and growth of the warm core of Karl are influenced by

661   both asymmetric and axisymmetric processes. The TA and especially HIWRAP data

662   showed that convective induced descent on the inner-edge of the eyewall and in the eye

663   itself was significant, which helps to warm and dry the eye over time. In addition, in one

664   GH overpass the HIWRAP and HAMSR data revealed that turbulent mixing between the

665   eye and eyewall eroded the reflectivity on a local scale. These processes contribute

666   largely to an asymmetric development of the eye and warm core of Karl. During the

667   vortex response phase where the convective bursts are less pronounced and

668   axisymmetrization of the convective anomalies is dominant, the development of the eye

669   has a clear axisymmetric signal shown by the time series of HIWRAP data.

670   Taking in the full scope of the data and analysis, we conclude that the convective

671   bursts played an important role in the rapid intensification of Hurricane Karl (2010).

672   These results build on a large body of evidence supporting the role of convective bursts

673 and their axisymmetric and asymmetric dynamical pathways to the TC intensification

674 problem. We also note that the routine use of the Global Hawk aircraft carrying the

675 HIWRAP and HAMSR instruments for the study of TC evolution and operational

676 forecasting in the future appears promising if the function of the aircraft can mirror that

677 conducted during GRIP.

678

690

691 <div align="center">APPENDIX</div>

692 **Comparison of HIWRAP wind retrievals to flight level data**

693 The HIWRAP radar participated in the NASA Hurricane and Severe Storm Sentinel

694 (HS3) field campaign between the years 2012 – 2014 to study hurricane evolution. As

695 part of this experiment, a coordinated flight between the Global Hawk and the NOAA P3

696   aircraft on September 25, 2013 allowed for the opportunity to validate the HIWRAP wind

697   retrievals with flight level wind data. The aircraft sampled the end of a large-scale frontal

698   system with a mix of stratiform and weak convective precipitation.

699   To make the comparisons, all HIWRAP data with a time offset of < 10 minutes and

700   space offset of < 1 km from the P3 aircraft and with reflectivity > 5 dBZ are retained.

701   These data are then interpolated to the locations of the flight level measurements (height

702   of ~ 2 km). In an attempt to match the along-track sampling of the flight level winds (1

703   Hz or ~ 100 – 150 m for a typical P3 airspeed) with the HIWRAP wind retrieval grid (1

704   km) a 10-point running mean filter is applied to the flight level winds.

705   Figure A1 shows a scatter plot of the horizontal wind speed error, defined as

706 |HIWRAP – P3 flight level|, vs. the flight level horizontal wind speed. In this figure,

707   HIWRAP Ku band data is shown. There is a clear trend of lower errors for higher wind

708   speeds. For all the points in Fig. A1 (N = 2727) the RMSE for wind speed and direction

709   (not shown) is 7.8 m s^{-1} and 27°, respectively. When considering points where the wind

710   speed is > 10 m s^{-1} (N = 1077) the RMSE for wind speed and direction is 1.3 m s^{-1} and

711   19°, respectively. These errors are slightly lower for Ka band data likely due to the

712   higher signal-to-noise ratios when compared to Ku band. For example, when the wind

713   speed is > 10 m s^{-1} (N = 1321) the RMSE for wind speed and direction using Ka band

714   data is 1.1 m s^{-1} and 15°. No clear reflectivity dependence is observed in Fig. A1, but the

715   values give an indication of the intensity of precipitation sampled.

716   Coordination between the Global Hawk and NOAA P3 aircraft also occurred for one

717   overpass of Hurricane Karl during GRIP on September 16, 2010 at ~ 2040 UTC. The

718   same procedures described above were applied to this data. The flight level

719   measurements were located between 3.5 and 3.8 km height and the time offset between

720   the aircraft was ~ 2 – 3 minutes. Figure A2 shows these comparison results for the same

721   kind of scatter plot as that in Fig. A1. A trend for lower errors with increasing wind

722   speeds is not observed with the range of values sampled here, but a slight indication of

723   lower errors for higher reflectivity values is somewhat apparent. For all the points in Fig.

724   A2 (N = 239) the RMSE for wind speed and direction (not shown) is 4.0 m s^{-1} and 11°,

725   respectively.

726

727

728

729

730

731

732

733

734

735

736

737

738

739

740

741

742   References

743

744   Braun, S., M. T. Montgomery, and Z. Pu, 2006: High-resolution simulation of

745   Hurricane Bonnie (1998). Part I: The organization of eyewall vertical motion. *J.*

746   *Atmos. Sci.*, **63**, 19–42.

747

748   Braun, S., R. Kakar, E. Zipser, G. Heymsfield, C. Albers, S. Brown, S. Durden, S.

749   Guimond, J. Halverson, A. Heymsfield, S. Ismail, B. Lambrigtsen, T. Miller, S.

750   Tanelli, J. Thomas and J. Zawislak, 2013: NASA's Genesis and Rapid Intensification

751   Processes (GRIP) field experiment. *Bull. Amer. Meteor. Soc.*, **94,** 345 – 363.

752

753   Brown, S.T., Lambrigtsen, B., Denning, R.F., Gaier, T., Kangaslahti, P., Lim, B.H.,

754   Tanabe, J.M., Tanner, A.B., 2011: The High-Altitude MMIC Sounding Radiometer

755   for the Global Hawk Unmanned Aerial Vehicle: Instrument description and

756   performance. *IEEE Transactions on Geoscience and Remote Sensing*, doi:

757   10.1109/TGRS.2011.2125973.

758

759   Cram, T.A., J. Persing, M. T. Montgomery, and S.A. Braun, 2007: A lagrangian

760   trajectory view on transport and mixing processes between the eye, eyewall and

761   environment using a high-resolution simulation of Hurricane Bonnie (1998). *J. Atmos.*

762   *Sci.*, **64,** 1835 – 1856.

763

764   Emanuel, K.A., 1986: An air-sea interaction theory for tropical cyclones. Part I: Steady-

765   state maintenance. *J. Atmos. Sci.*, **43,** 2044-2061.

766

767   Gamache, J.F., F.D. Marks, and F. Roux, 1995: Comparison of three airborne Doppler

768   sampling techniques with airborne in situ wind observations in Hurricane Gustav

769   (1990). *J. Atmos. Oceanic Technol.*, **12,** 171 – 181.

770

771   Gamache, J.F., 1997: Evaluation of a fully three-dimensional variational Doppler

772   analysis technique. Preprints, *28th Conf. on Radar Meteorology,* Austin, TX, Amer.

773   Meteor. Soc., 422 – 423.

774

775   Gamache, J.F., 2005: Real-time dissemination of hurricane wind fields determined from

776   airborne Doppler radar data. National Hurricane Center, 38 pp. [Available online at

777   http://www.nhc.noaa.gov/jht/2003-2005reports/DOPLRgamache_JHTfinalreport.pdf]

778

779   Guimond, S. R., G. M. Heymsfield, and F. J. Turk, 2010: Multiscale observations of

780   Hurricane Dennis (2005): The effects of hot towers on rapid intensification. *J. Atmos.*

781   *Sci.*, **67**, 633–654.

782

783   Guimond, S.R., L. Tian, G.M. Heymsfield, and S.J. Frasier, 2014: Wind retrieval

784   algorithms for the IWRAP and HIWRAP airborne Doppler radars with applications to

785   hurricanes. *J. Atmos. Oceanic Technol.*, **31,** 1189 – 1215.

786

787   Guimond, S.R., J.M. Reisner, S. Marras, and F.X. Giraldo, 2016: The impacts of

788   numerical schemes on asymmetric hurricane intensification. *J. Atmos. Sci.*, submitted.

789

790   Hendricks, E.A., B.D. McNoldy, and W.H. Schubert, 2012: Observed inner-core

791   structural variability in Hurricane Dolly (2008). *Mon. Wea. Rev.*, **140,** 4066 – 4077.

792

793   Hendricks, E.A., W.H. Schubert, Y. Chen, H. Kuo and M.S. Peng, 2014: Hurricane

794   eyewall evolution in a forced shallow-water model. *J. Atmos. Sci.*, **71,** 1623 – 1643.

795

796   Heymsfield, G. M., J. B. Halverson, J. Simpson, L. Tian, and T. P. Bui, 2001: ER-2

797   Doppler radar investigations of the eyewall of Hurricane Bonnie during the

798   Convection and Moisture Experiment-3. *J. Appl. Meteor.*, **40**, 1310–1330.

799

800   Houze, R.A., W.C. Lee, and M.M. Bell, 2009: Convective contribution to the genesis of

801   Hurricane Ophelia (2005). *Mon. Wea. Rev.*, **137,** 2778 – 2800.

802

803   Kaplan, J., and M. DeMaria, 2003: Large-scale characteristics of rapidly intensifying

804   tropical cyclones in the North Atlantic basin. *Wea. Forecasting*, **18,** 1093 – 1108.

805

806   Kelley, O. A., J. Stout, and J. B. Halverson, 2004: Tall precipitation cells in tropical

807   cyclone eyewalls are associated with tropical cyclone intensification. *Geophys. Res.*

808   *Lett.*, **31.**

809

810   Kossin, J.P., and W.H. Schubert, 2001: Mesovortices, polygonal flow patterns, and rapid

811   pressure falls in hurricane-like vortices. *J. Atmos. Sci.*, **58,** 2196 – 2209.

812

813   Li, L., G.M. Heymsfield, J. Carswell, D. Schaubert, M. Mclinden, J. Creticos, M. Perrine,

814   M. Coon, J. Cervantes, M. Vega, S. Guimond, L. Tian, and A. Emory, 2015: The

815   NASA High-altitude Imaging Wind and Rain Airborne Profiler (HIWRAP). *IEEE*

816   *Trans. Geosci. Remote Sens.*, **54,** 298 – 310.

817

818   Marks, F.D., 1985: Evolution and structure of precipitation in Hurricane Allen (1980).

819   *Mon. Wea. Rev.*, **113,** 909 – 930.

820

821   Molinari, J. and D. Vollaro, 2010: Rapid Intensification of a Sheared Tropical

822   Storm. *Mon. Wea. Rev.*, **138**, 3869–3885.

823

824   Montgomery M. T., and R. J. Kallenbach, 1997: A theory for vortex Rossby waves and

825   its application to spiral bands and intensity changes in hurricanes. *Quart. J. Roy.*

826   *Meteor. Soc.*, **123**, 435–465.

827

828   Montgomery, M. T., M. Nicholls, T. Cram, and A. Saunders, 2006: A vortical hot

829   tower route to tropical cyclogenesis. *J. Atmos. Sci.*, **63**, 355–386.

830

831   Nolan, D.S., and L.D. Grasso, 2003: Three-dimensional, nonhydrostatic perturbations to

832   balanced, hurricane-like vortices. Part II: Symmetric response and nonlinear

833   simulations. *J. Atmos. Sci.*, **60,** 2717-2745.

834

835   Nolan, D.S., Y. Moon, and D.P.Stern, 2007: Tropical cyclone intensification from

836   asymmetric convection: Energetics and efficiency. *J. Atmos. Sci.*, **64,** 3377-3405.

837

838   Persing, J., M.T. Montgomery, J.C. McWilliams, R.K. Smith, 2013: Asymmetric and

839   axisymmetric dynamics of tropical cyclones. *Atmos. Chem. Phys.*, **13,** 12299 – 12341.

840

841   Reasor, P.D., M.T. Montgomery, F.D. Marks Jr., and J.F. Gamache, 2000: Low-

842   wavenumber structure and evolution of the hurricane inner core observed by airborne

843   dual-Doppler radar. *Mon. Wea. Rev.*, **128,** 1653 – 1680.

844

845   Reasor, P.D., M.T. Montgomery, and L.F. Bosart, 2005: Mesoscale observations of the

846   genesis of Hurricane Dolly (1996). *J. Atmos. Sci.*, **62,** 3151 – 3171.

847

848   Reasor, P. D., M. D. Eastin, and J. F. Gamache, 2009: Rapidly intensifying Hurricane

849   Guillermo (1997). Part I: Low-wavenumber structure and evolution. *Mon. Wea. Rev.*,

850   **137,** 603–631.

851

852   Rinehart, B., H. Fuelberg, R. Blaskeslee, D. Mach, A. Heymsfield, A. Bansemer, S.L.

853   Durden, S. Tanelli, G. Heymsfield, and B. Lambrigtsen, 2014: Understanding the

854   relationships between lightning, cloud microphysics, and airborne radar derived storm

855   structure during Hurricane Karl (2010). *Mon. Wea. Rev.*, **142,** 590 – 605.

856

857   Rogers, R.F., P.D. Reasor, and S. Lorsolo, 2013: Airborne Doppler observations of the

858   inner-core structural differences between intensifying and steady-state tropical

859   cyclones. *Mon. Wea. Rev.*, **141,** 2970 – 2991.

860

861   Rogers, R. F., P.D. Reasor, and J.A. Zhang, 2015: Multiscale structure and evolution of

862   Hurricane Earl (2010) during rapid intensification. *Mon. Wea. Rev.*, **143,** 536 – 562.

863

864   Rotunno, R., and K.A. Emanuel, 1987: An air-sea interaction theory for tropical

865   cyclones. Part II: Evolutionary study using a nonhydrostatic axisymmetric numerical

866   model. *J. Atmos. Sci.,* **44,** 542-561.

867

868   Rozoff, C.M., J.P. Kossin, W.H. Schubert, and P.J. Mulero, 2009: Internal control of

869   hurricane intensity: The dual nature of potential vorticity mixing. *J. Atmos. Sci.*, **66,**

870   133 – 147.

871

872   Schubert, W.H., and J.J. Hack, 1982: Inertial stability and tropical cyclone development.

873   *J. Atmos. Sci.*, **39,** 1687 – 1697.

874

875   Schubert, W.H., M.T. Montgomery, R.K. Taft, T.A. Guinn, S.R. Fulton, J.P. Kossin, and

876   J.P. Edwards, 1999: Polygonal eyewalls, asymmetric eye contraction, and potential

877   vorticity mixing in hurricanes. *J. Atmos. Sci.*, **56,** 1197 – 1223.

878

879   Shapiro, L.J. and H.E. Willoughby, 1982: The response of balanced hurricanes to local

880   sources of heat and momentum. *J. Atmos. Sci.*, **39,** 378 – 394.

881

882   Simpson, J., J. B. Halverson, B. S. Ferrier, W. A. Petersen, R. H. Simpson, R. Blakeslee,

883   and S. L. Durden, 1998: On the role of "hot towers" in tropical cyclone formation.

884   *Meteor. Atmos. Phys.*, **67,** 15–35.

885

886   Steranka, J., E.B. Rodgers, and R.C. Gentry, 1986: The relationship between satellite-

887   measured convective bursts and tropical cyclone intensification. *Mon. Wea. Rev.*, **114,**

888   1539 – 1546.

889

890   Stevenson, S.N., K.L. Corbosiero, and J. Molinari, 2014: The convective evolution and

891   rapid intensification of Hurricane Earl (2010). *Mon. Wea. Rev.*, **142,** 4364 – 4380.

892

893   Stewart, S., 2010: Tropical cyclone report: Hurricane Karl 14 – 18 September 2010.

894   National Hurricane Center, 17 pp. [Available online at

895   http://www.nhc.noaa.gov/2010atlan.shtml].

896

897   Willoughby, H.E., and M.B. Chelmow, 1982, Objective determination of hurricane tracks

898   from aircraft observations. *Mon. Wea. Rev.*, **110,** 1298 – 1305.

899

900

901

902

903 FIGURE CAPTIONS

904 1. Best track of Hurricane Karl (2010) starting from 0000 UTC 14 September with

905 intensity classifications marked every six hours. The days in September at 0000 UTC are

906 also shown. The green circles denote tropical depression status, open hurricane symbols

907 are tropical storm and closed hurricane symbols are hurricane status with the category

908 listed in the center. The inset shows the time series of maximum surface wind speed in m

909 s^{-1} with the Global Hawk flight bracketed with the black lines.

910

911 2. A sequence of GOES IR images of Hurricane Karl (2010) in the Bay of Campeche

912 during an RI episode spanning the GH flights into the storm. The times shown are (a)

913 1845 UTC 16 September, (b) 2215 UTC 16 September, (c) 0140 UTC 17 September and

914 (d) 0501 UTC 17 September. The white arrow in (a) denotes the environmental vertical

915 wind shear vector valid over the time interval. The star represents the estimated storm

916 center. The track of the GH $\pm$ 2 h from the satellite time stamp is shown in white with

917 the large numbers denoting the hour (UTC).

918

919 3. Composite analysis of HIWRAP data averaged over the total Global Hawk sampling

920 interval (12 – 13 h) at 2 km height for (a) Ku band reflectivity (dBZ) and horizontal wind

921 vectors and (b) horizontal wind speeds (m s^{-1}). The white arrows in (b) highlight

922 anomalously large wind speeds in the eyewall discussed in the text.

923

924 4. As in Fig. 3 only at 8 km height and zoomed in on the inner-core of Karl. The large,

925 gray arrow in (a) is the large-scale vertical wind shear vector valid for this time interval

926   with a value of ~ 5 m s^{-1}. The thick white arrows in (a) show the locations of low-level

927   (2 km) anomalously large wind speeds in the eyewall (see Fig. 3b). The white circle in

928   (a) shows the location of the low-level (2 km), time and azimuthally averaged RMW.

929

930   5. NOAA P3 flight through the inner-core of Hurricane Karl (2010) centered at ~ 1842

931   UTC 16 September showing (a) LF C-band reflectivity at 3.7 km height overlaid with TA

932   derived winds at 4 km height and (b) TA derived radial wind speeds averaged between 1

933   – 4 km height overlaid with perturbation wind vectors averaged over the same interval.

934   The white arrows in (b) highlight features discussed in the text. The gray line in (b)

935   marks the eye-eyewall interface using the gradient in LF reflectivity. The "C" and "A"

936   letters in (b) denote the centers of cyclonic and anti-cyclonic mesovortex circulations,

937   respectively.

938

939   6. Global Hawk overpass of the inner-core of Hurricane Karl (2010) between 1853 –

940   1919 UTC 16 September showing (a) HAMSR 54 GHz Tbs (K) and (b) HIWRAP Ku

941   band reflectivity (dBZ). In both figures, horizontal wind vectors from HIWRAP are

942   overlaid and the analysis level is 2 km height. The white arrows in (a) highlight a feature

943   discussed in the text. The reference vector in (a) applies to both figures. Note that the

944   azimuthal mean RMW at this time and level is ~ 30 km.

945

946   7. HIWRAP vertical cross sections at nadir through the storm center in the North-South

947   direction for the Global Hawk overpass between 1853 – 1919 UTC 16 September. The

948   data shown is (a) Ku band reflectivity (dBZ), (b) meridional (radial) winds (m s^{-1}), (c)

949 vertical winds (m s^{-1}) and (d) vertical vorticity (s^{-1}). The large gray arrows in (b) and (c)

950 highlight features discussed in the text.

951

952 8. NOAA P3 flight through the inner-core of Hurricane Karl (2010) centered at ~ 1930

953 UTC 16 September showing (a) LF reflectivity at 3.6 km height overlaid with TA derived

954 winds at 4 km height and (b) TA derived divergence (s^{-1}) averaged between 1 – 4 km

955 height overlaid with perturbation winds averaged over the same interval. The gray line in

956 (b) marks the eye-eyewall interface using the gradient in LF reflectivity. The "C" and

957 "A" letters in (b) denote the centers of cyclonic and anti-cyclonic mesovortex

958 circulations, respectively.

959

960 9. As in Fig. 6a, but for the GH overpass between 1938 – 1957 UTC 16 September. The

961 large white circle denotes the azimuthally averaged RMW at 2 km height and the white

962 dot is the storm center.

963

964 10. As in Fig. 7 except for the Global Hawk overpass between 1938 – 1957 UTC 16

965 September. The data shown is (a) Ku band reflectivity (dBZ), (b) radial winds (m s^{-1}), (c)

966 vertical winds (m s^{-1}) and (d) tangential winds (m s^{-1}). The gray arrows in (b) and (c)

967 highlight features discussed in the text.

968

969 11. As in Fig. 8, only for the NOAA P3 transect centered at ~ 2042 UTC 16 September.
970

971

972   12. As in Fig. 6a, but for the GH overpass between 2009 – 2055 UTC 16 September with

973   a center crossing at ~ 2040 UTC. The large white circle denotes the azimuthally

974   averaged RMW at 2 km height and the white dot is the storm center. The gray box shows

975   the region where data are averaged in the y-direction for subsequent figures. The "C"

976   letter denotes the center of a mesovortex cyclonic circulation.

977

978   13. Vertical cross sections of radar reflectivity averaged between ~ 0 – 6 km in the +y-

979   direction (see Fig. 12) from (a) HIWRAP Ku band data valid at ~ 2040 UTC 16

980   September (b) NOAA P3 X band data valid at ~ 2042 UTC 16 September. Note that

981   there is no data on the right side of (a) due to the HIWRAP coverage and cross section

982   cut.

983

984   14. As in Fig. 13, only for radial winds. The gray line denotes the western eye-eyewall

985   interface using the gradient in reflectivity.

986

987   15. As in Fig. 14, only for vertical winds. The large gray arrows highlight features

988   discussed in the text.

989

990   16. HIWRAP vertical cross sections of Ku band reflectivity (shading; dBZ) and

991   tangential winds (contours; m s^{-1}) at nadir for the Global Hawk overpasses on 17

992   September centered at (a) 0012 UTC in southeast to northwest direction (b) 0345 UTC in

993   southwest to northeast direction (c) 0550 UTC in southeast to northwest direction and (d)

994   0805 UTC in southeast to northwest direction.

995

996   17. Conceptual diagram highlighting the measurements and analysis from the HIWRAP,

997   HAMSR and P3 instruments during the Hurricane Karl (2010) sampling. The arrows

998   represent the mesoscale flow with red indicating anomalously warm, buoyant air.

999

1000   A1. Scatter plot of HIWRAP horizontal wind speed errors (|HIWRAP – P3 flight level|)

1001   vs. P3 flight level wind speeds for the coordinated flight during HS3 on 25 Sept. 2013.

1002   The points are colored by HIWRAP Ku band reflectivity. Note the HIWRAP winds are

1003   computed using Ku band Doppler velocities. See text for more details.

1004

1005   A2. As in Fig. A1, only for the coordinated flight during GRIP (sampling of Hurricane

1006   Karl on 16 Sept. 2010 at ~ 2040 UTC). The points are colored by HIWRAP Ku band

1007   reflectivity. Note the HIWRAP winds are computed using a combination of Ku and Ka

1008   band Doppler velocities. See text for more details.

1009
1010
1011
1012
1013
1014
1015
1016
1017
1018
1019
1020
1021
1022
1023
1024
1025
1026

1027
1028
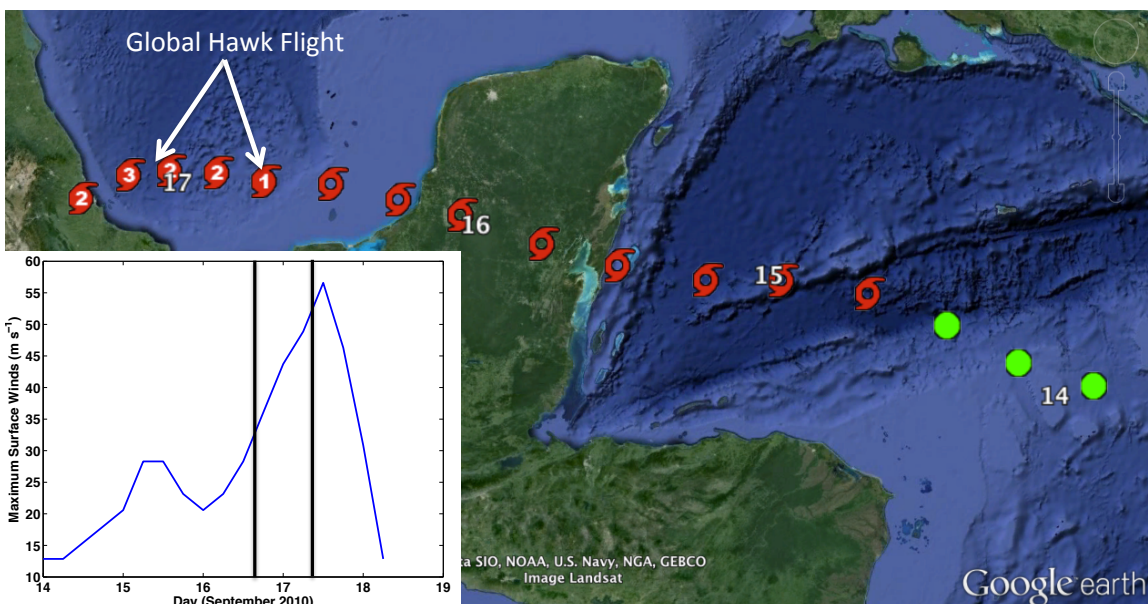
1029
1030
1031 Figure 1. Best track of Hurricane Karl (2010) starting from 0000 UTC 14 September
1032 with intensity classifications marked every six hours. The days in September at 0000
1033 UTC are also shown. The green circles denote tropical depression status, open hurricane
1034 symbols are tropical storm and closed hurricane symbols are hurricane status with the
1035 category listed in the center. The inset shows the time series of maximum surface wind
1036 speed in m s^{-1} with the Global Hawk flight bracketed with the black lines.
1037
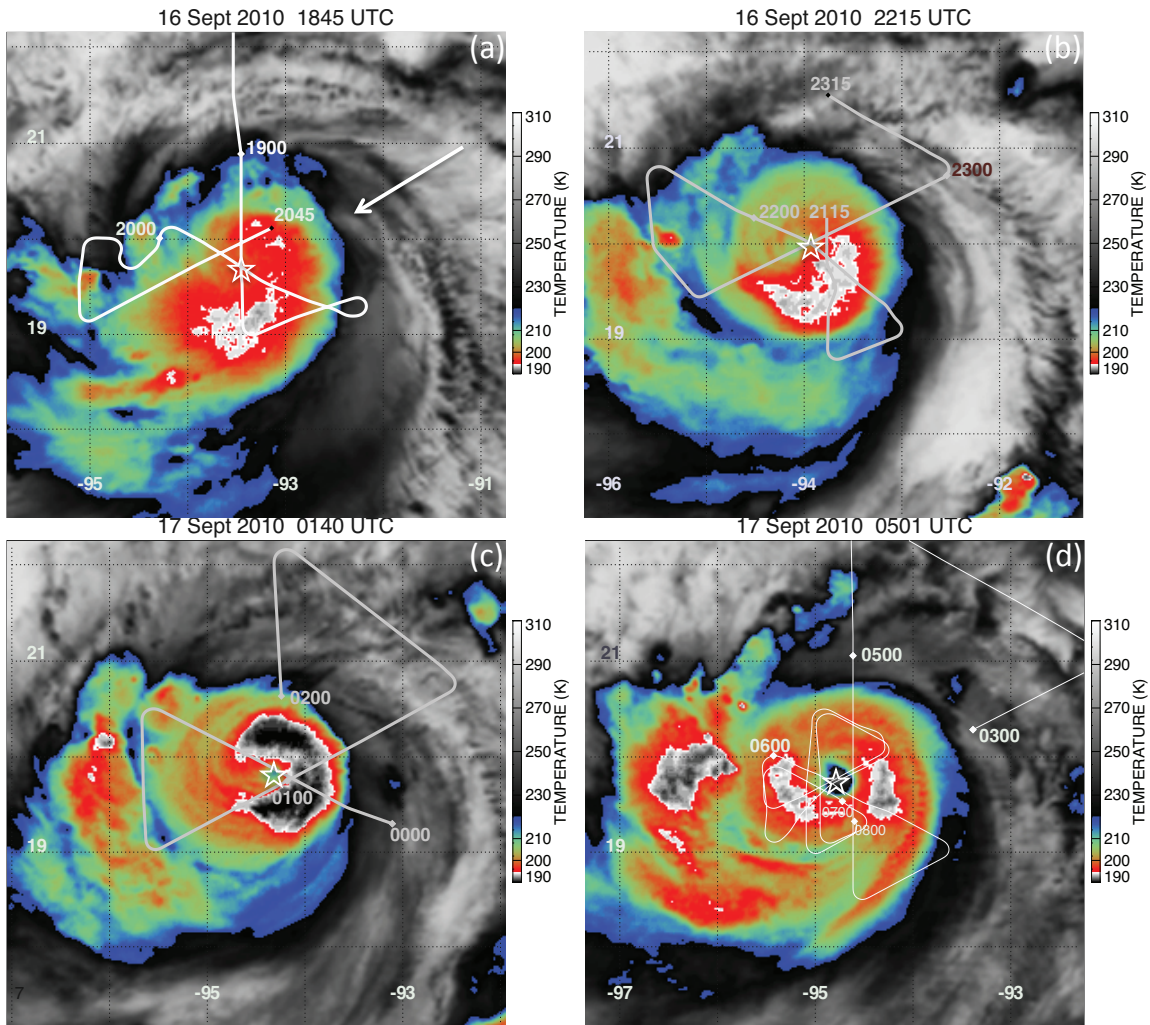
Figure 2. A sequence of GOES IR images of Hurricane Karl (2010) in the Bay of Campeche during an RI episode spanning the GH flights into the storm. The times shown are (a) 1845 UTC 16 September, (b) 2215 UTC 16 September, (c) 0140 UTC 17 September and (d) 0501 UTC 17 September. The white arrow in (a) denotes the environmental vertical wind shear vector valid over the time interval. The star represents the estimated storm center. The track of the GH ± 2 h from the satellite time stamp is shown in white with the large numbers denoting the hour (UTC).
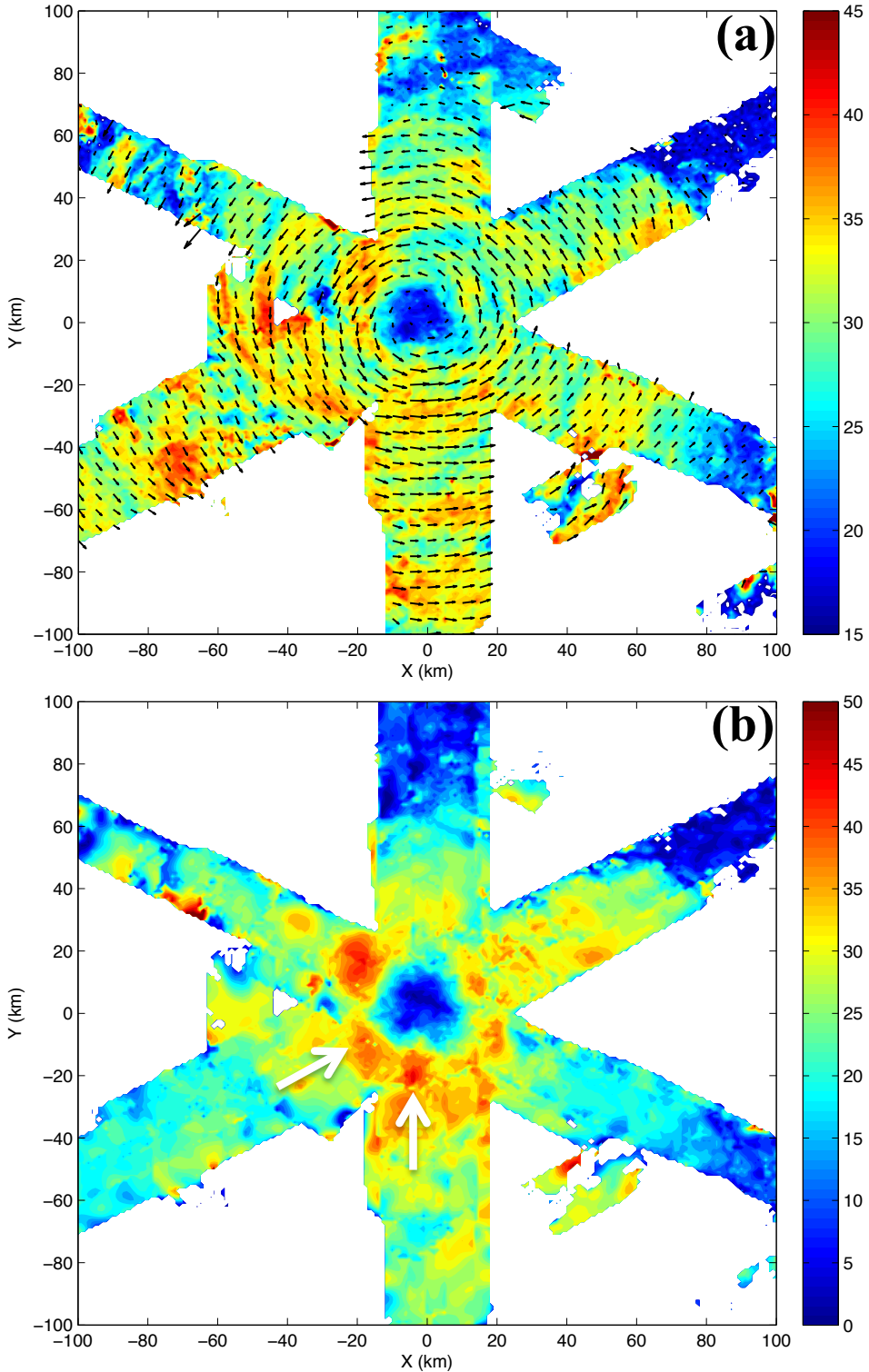
1058
1059   Figure 3. Composite analysis of HIWRAP data averaged over the total Global Hawk
1060   sampling interval (12 − 13 h) at 2 km height for (a) Ku band reflectivity (dBZ) and
1061   horizontal wind vectors and (b) horizontal wind speeds (m s^{-1}). The white arrows in (b)
1062   highlight anomalously large wind speeds in the eyewall discussed in the text.
1063
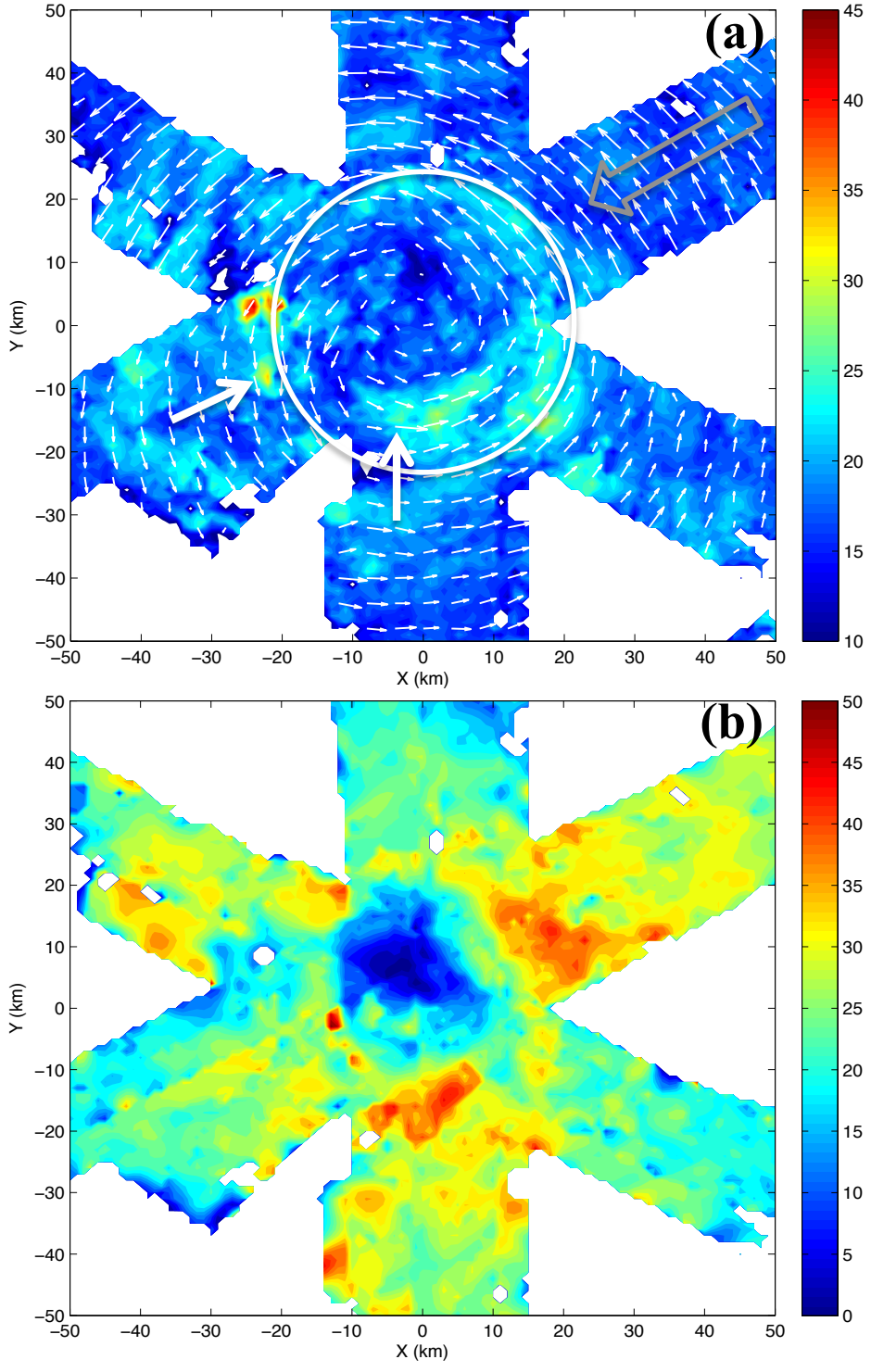
1064
1065 Figure 4. As in Fig. 3 only at 8 km height and zoomed in on the inner-core of Karl. The
1066 large, gray arrow in (a) is the large-scale vertical wind shear vector valid for this time
1067 interval with a value of ~ 5 m s^{-1}. The thick white arrows in (a) show the locations of
1068 low-level (2 km) anomalously large wind speeds in the eyewall (see Fig. 3b). The white
1069 circle in (a) shows the location of the low-level (2 km), time and azimuthally averaged
1070 RMW.
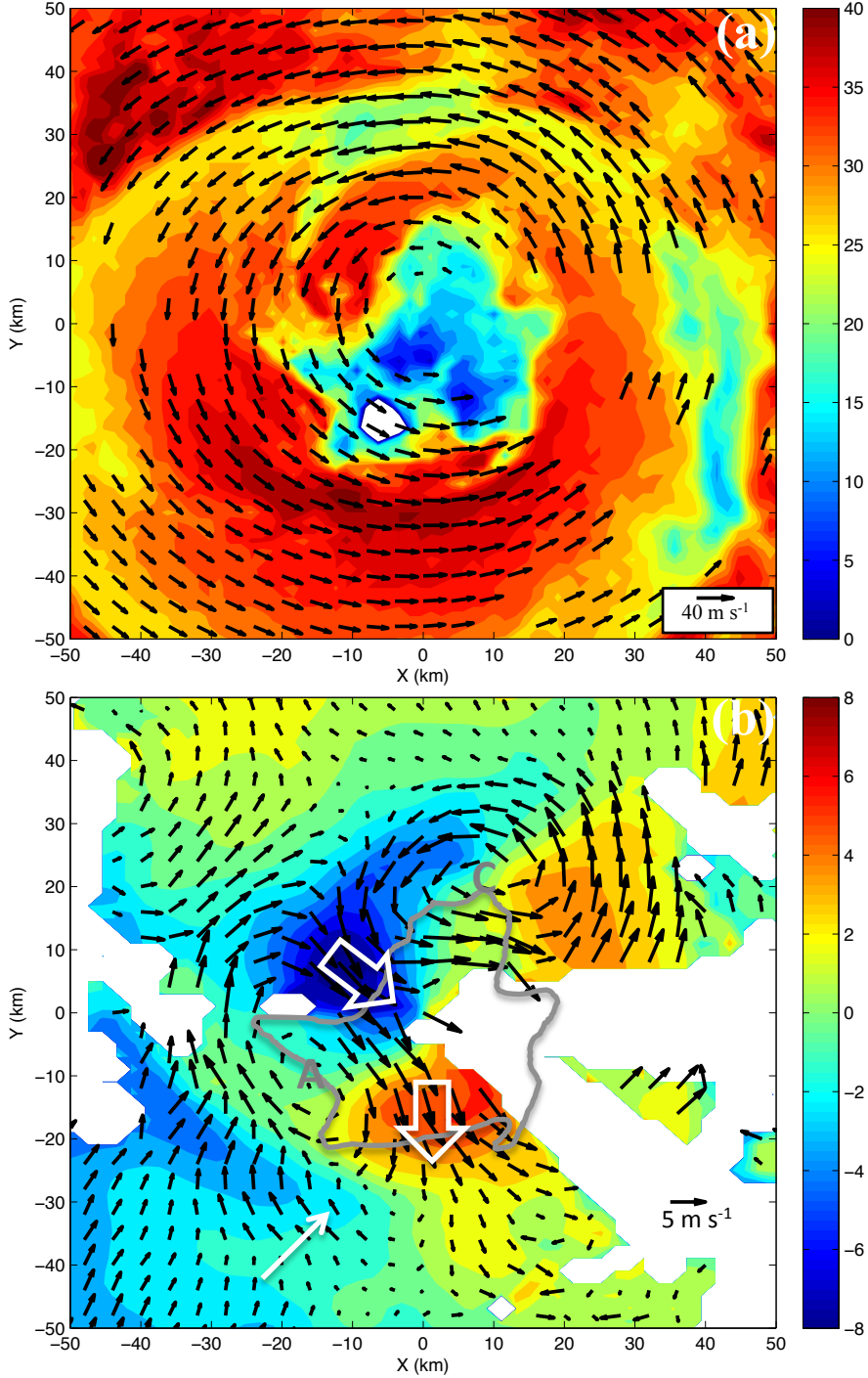
Figure 5. NOAA P3 flight through the inner-core of Hurricane Karl (2010) centered at ~ 1842 UTC 16 September showing (a) LF C-band reflectivity at 3.7 km height overlaid with TA derived winds at 4 km height and (b) TA derived radial wind speeds averaged between 1 – 4 km height overlaid with perturbation wind vectors averaged over the same interval. The white arrows in (b) highlight features discussed in the text. The gray line in (b) marks the eye-eyewall interface using the gradient in LF reflectivity. The "C" and "A" letters in (b) denote the centers of cyclonic and anti-cyclonic mesovortex circulations, respectively.
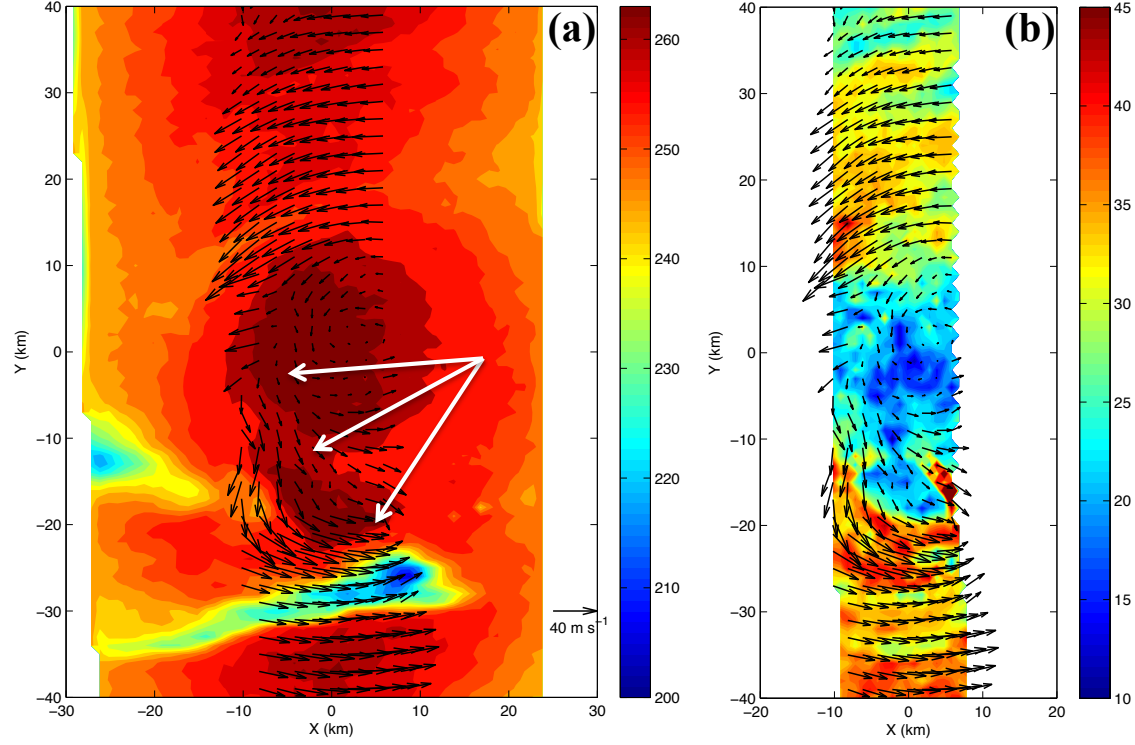
1084 Figure 6. Global Hawk overpass of the inner-core of Hurricane Karl (2010) between
1085 1853 – 1919 UTC 16 September showing (a) HAMSR 54 GHz Tbs (K) and (b) HIWRAP
1086 Ku band reflectivity (dBZ). In both figures, horizontal wind vectors from HIWRAP are
1087 overlaid and the analysis level is 2 km height. The white arrows in (a) highlight a
1088 protrusion of the warm core discussed in the text. The reference wind vector in (a)
1089 applies to both figures. Note that the azimuthal mean RMW at this time and level is ~ 30
1090 km.

1091
1092
1093
1094
1095
1096
1097
1098
1099
1100
1101
1102
1103
1104
1105
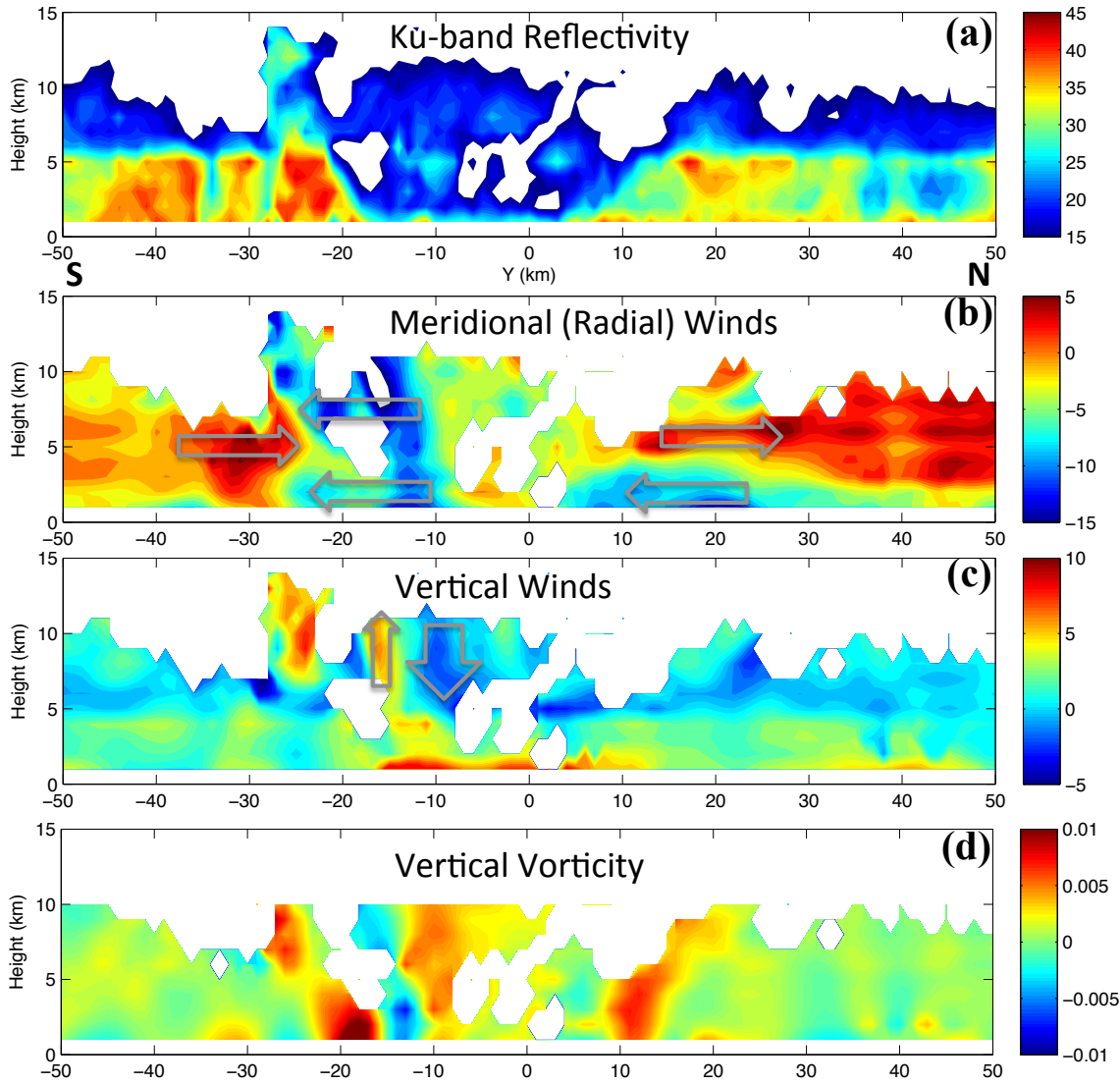
Figure 7. HIWRAP vertical cross sections at nadir through the storm center in the North-South direction for the Global Hawk overpass between 1853 – 1919 UTC 16 September. The data shown is (a) Ku band reflectivity (dBZ), (b) meridional (radial) winds (m s^{-1}), (c) vertical winds (m s^{-1}) and (d) vertical vorticity (s^{-1}). The large gray arrows in (b) and (c) highlight features discussed in the text.
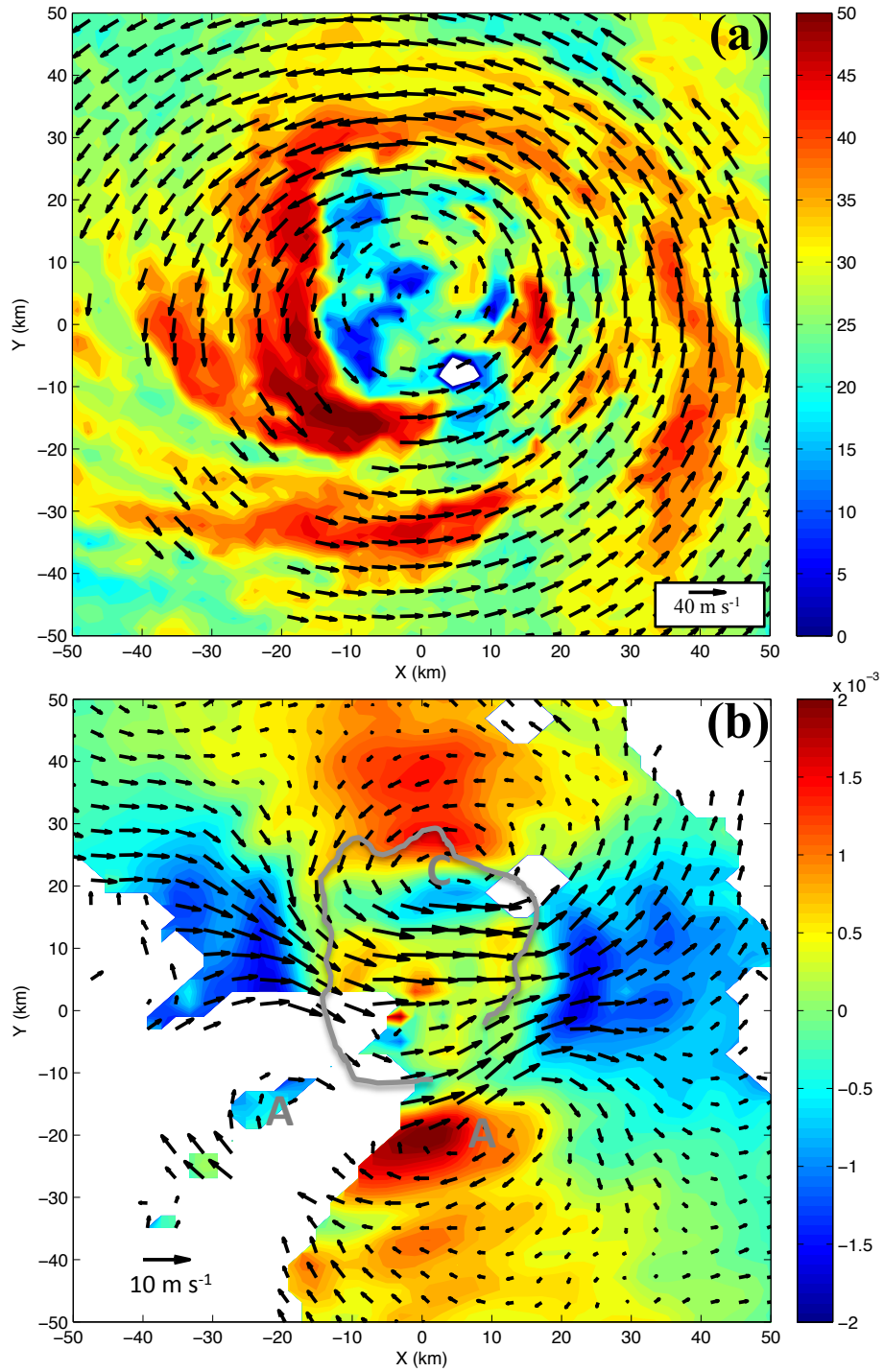
Figure 8. NOAA P3 flight through the inner-core of Hurricane Karl (2010) centered at ~ 1930 UTC 16 September showing (a) LF reflectivity at 3.6 km height overlaid with TA derived winds at 4 km height and (b) TA derived divergence (s^{-1}) averaged between $1-4$ km height overlaid with perturbation winds averaged over the same interval. The gray line in (b) marks the eye-eyewall interface using the gradient in LF reflectivity. The "C" and "A" letters in (b) denote the centers of cyclonic and anti-cyclonic mesovortex circulations, respectively.

1130
1131
1132
1133
1134
1135
1136
1137
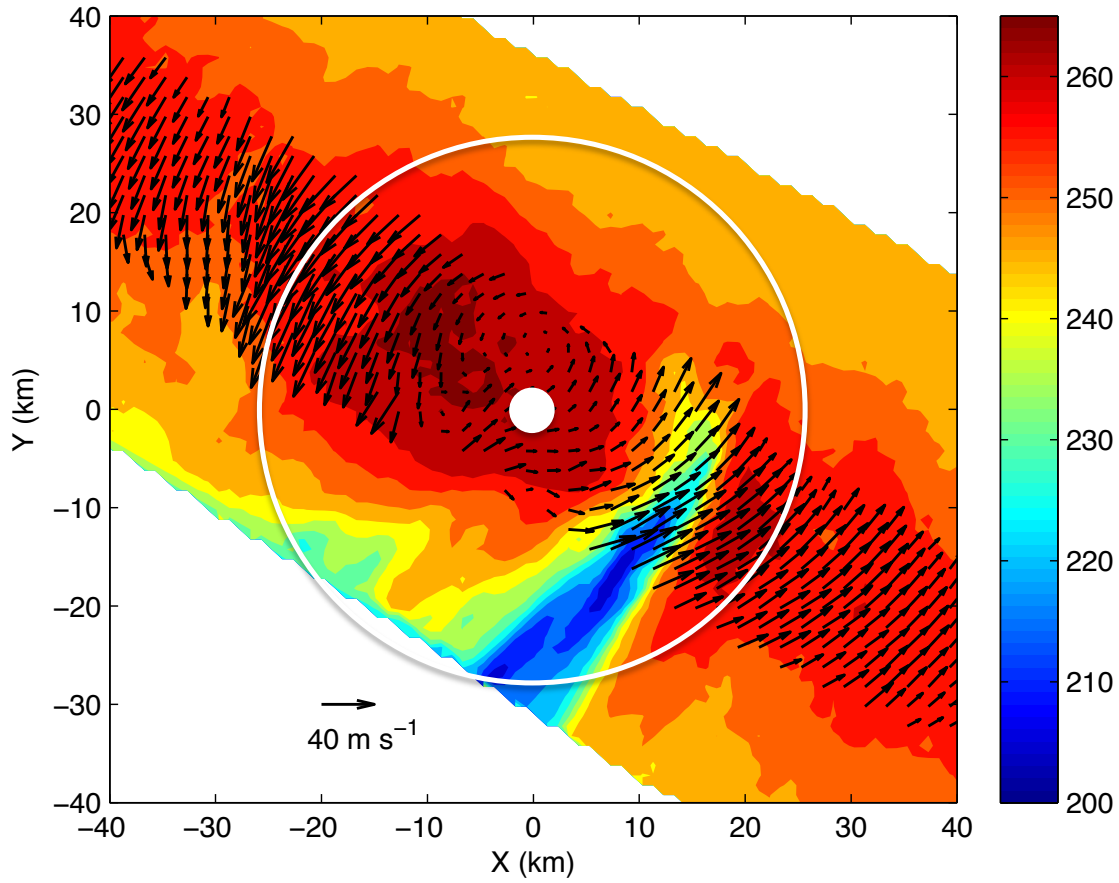
Figure 9. As in Fig. 6a, but for the GH overpass between 1938 – 1957 UTC 16 September. The large white circle denotes the azimuthally averaged RMW at 2 km height and the white dot is the storm center.

1143
1144
1145
1146
1147
1148
1149
1150
1151
1152
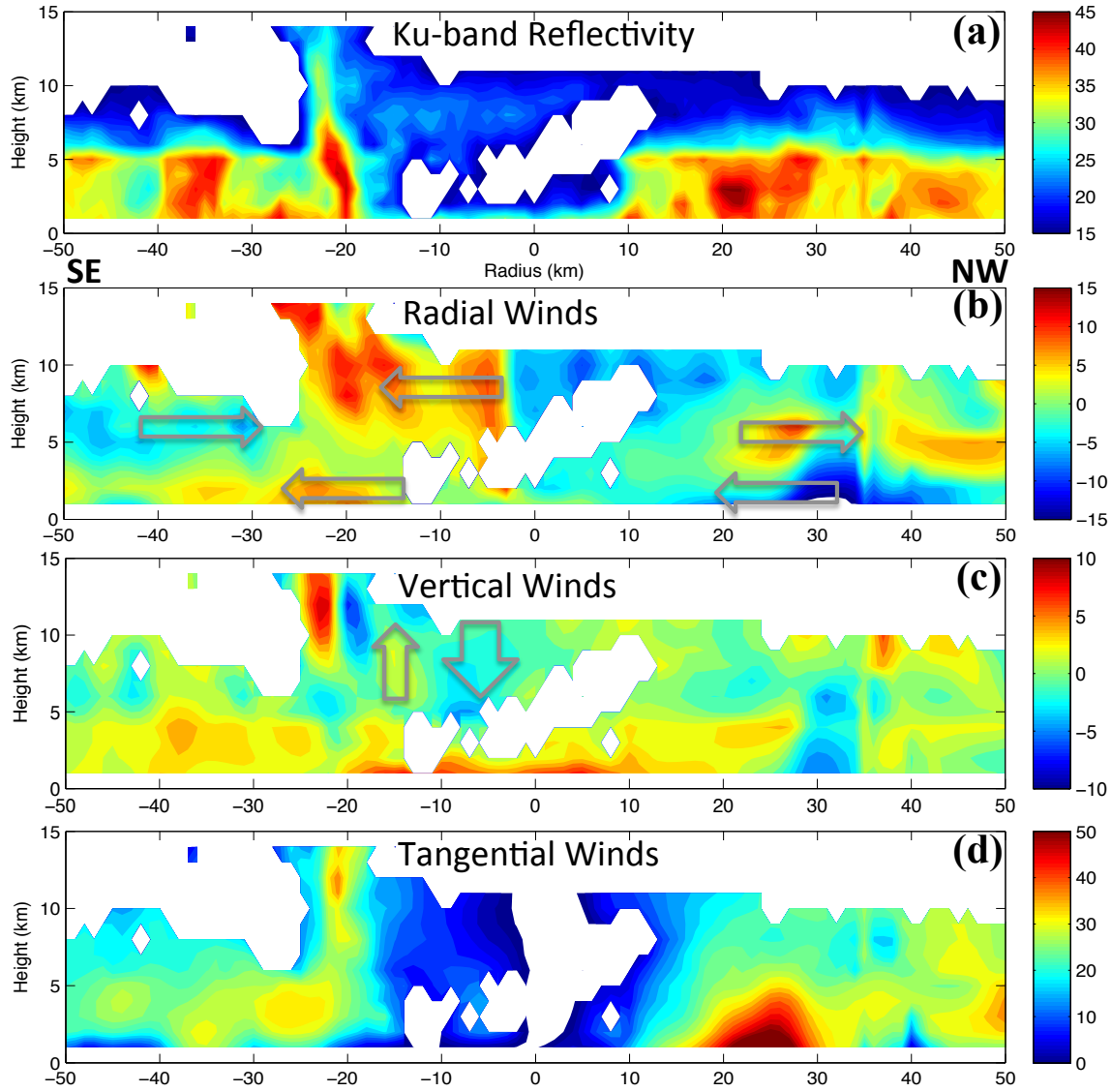
Figure 10. As in Fig. 7 except for the Global Hawk overpass between 1938 – 1957 UTC 16 September in the southeast (negative radius) to northwest (positive radius) direction. The data shown is (a) Ku band reflectivity (dBZ), (b) radial winds (m s^{-1}), (c) vertical winds (m s^{-1}) and (d) tangential winds (m s^{-1}). The gray arrows in (b) and (c) highlight features discussed in the text.
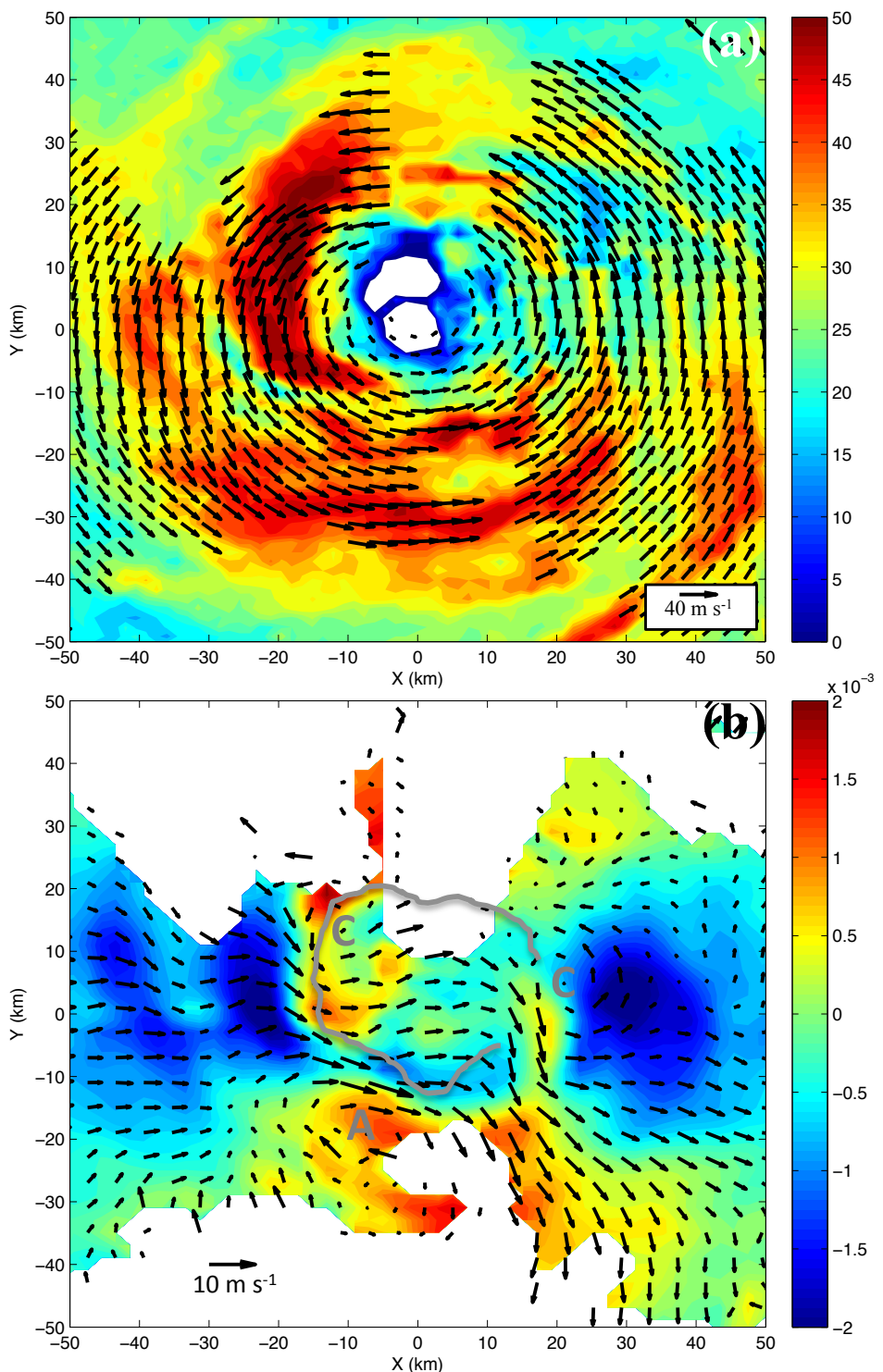
1160
Figure 11. As in Fig. 8, only for the NOAA P3 transect centered at ~ 2042 UTC 16
September.
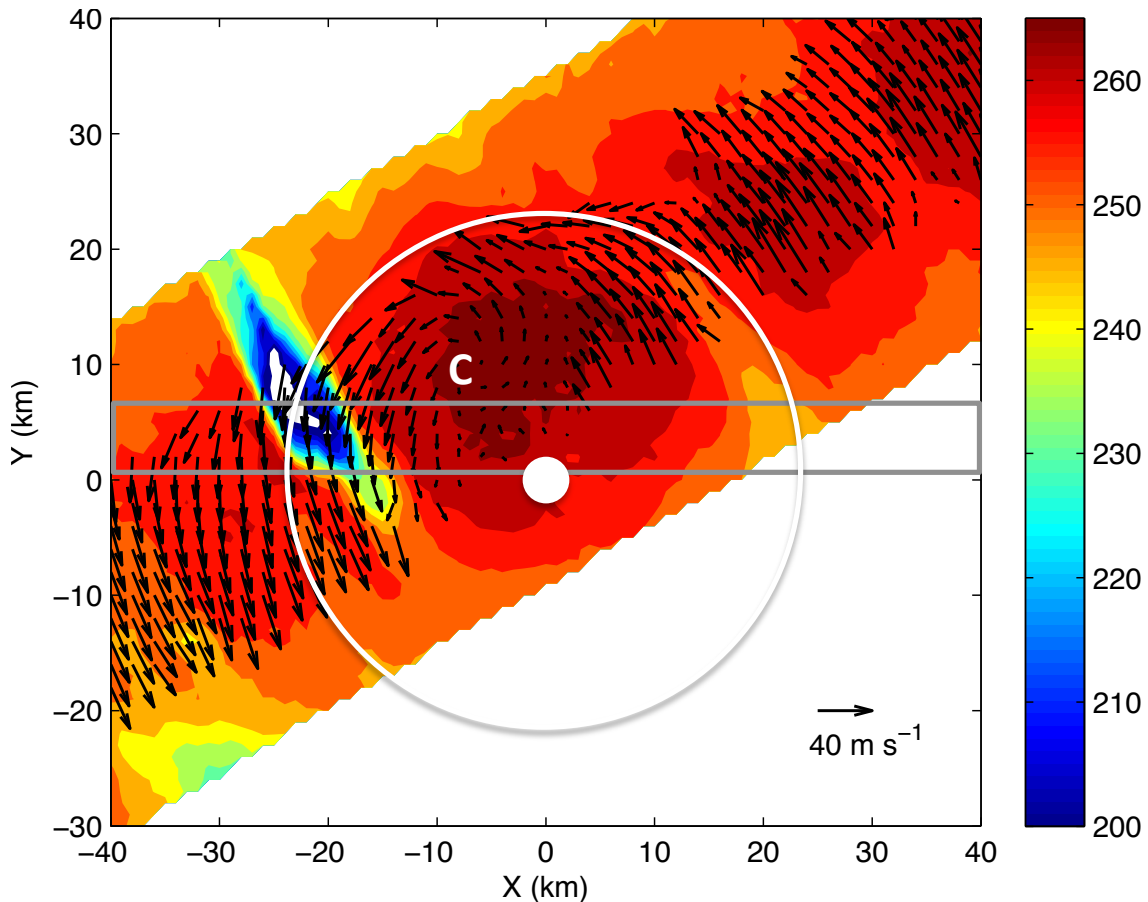
Figure 12. As in Fig. 6a, but for the GH overpass between 2009 – 2055 UTC 16
September with a center crossing at ~ 2040 UTC. The large white circle denotes the
azimuthally averaged RMW at 2 km height and the white dot is the storm center. The
gray box shows the region where data are averaged in the y-direction for subsequent
figures. The "C" letter denotes the center of a mesovortex cyclonic circulation.

1187
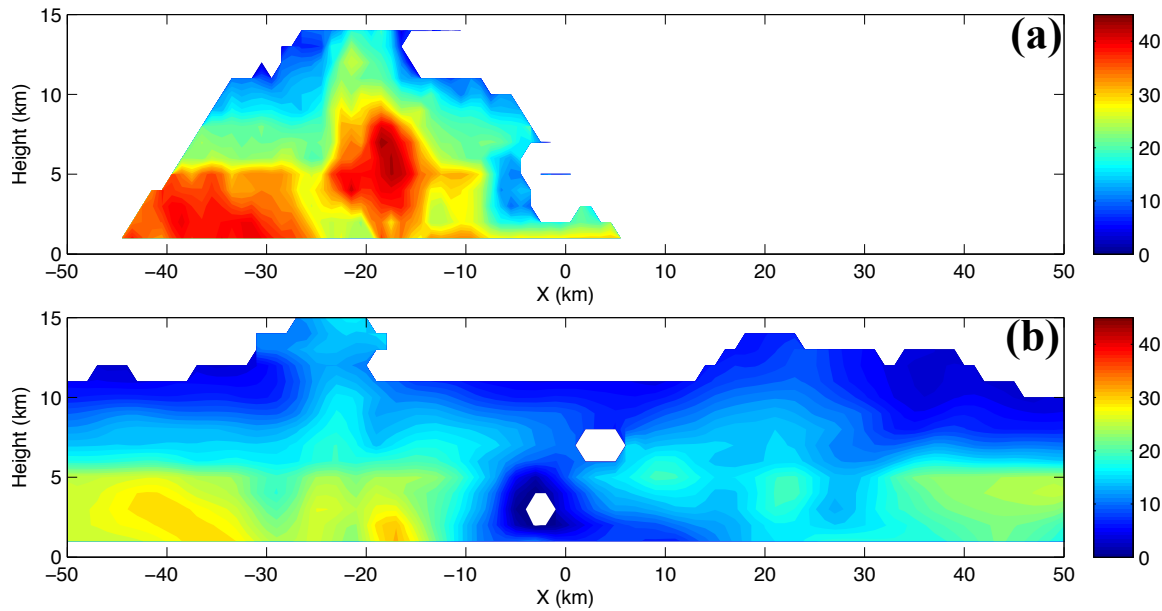
1188
1189 Figure 13. Vertical cross sections of radar reflectivity averaged between ~ 0 – 6 km in
1190 the +y-direction (see Fig. 12) from (a) HIWRAP Ku band data valid at ~ 2040 UTC 16
1191 September (b) NOAA P3 X band data valid at ~ 2042 UTC 16 September. Note that
1192 there is no data on the right side of (a) due to the HIWRAP coverage and cross section
1193 cut.
1194
1195
1196
1197
1198
1199
1200
1201
1202
1203
1204
1205
1206
1207
1208
1209
1210
1211
1212
1213
1214
1215
1216
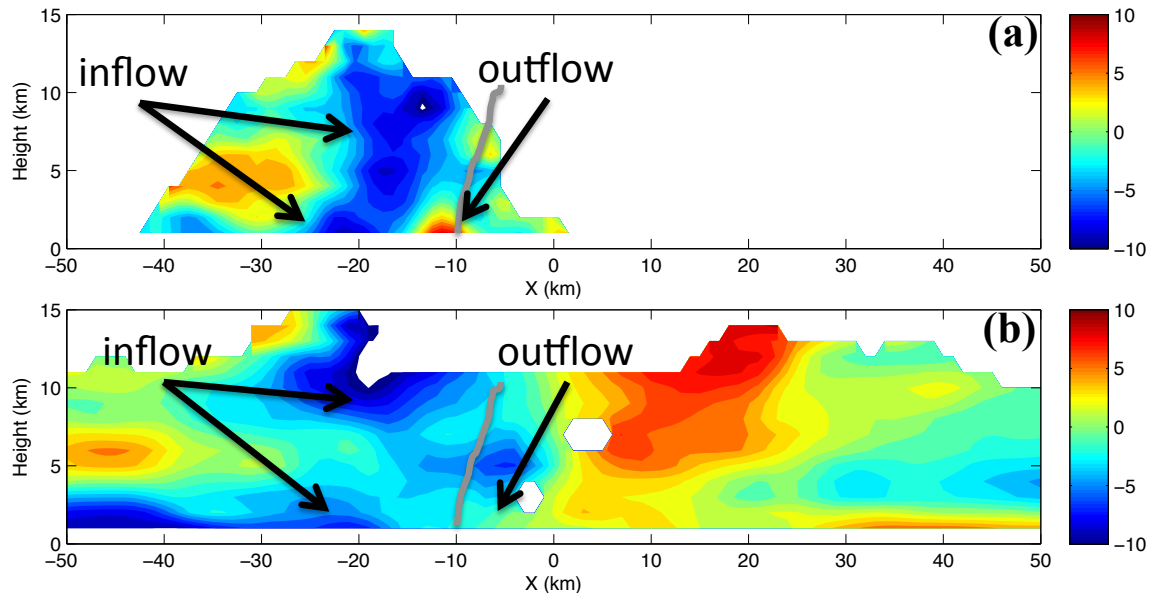
1222 Figure 14. As in Fig. 13, only for radial winds. The gray line denotes the western eye-
1223 eyewall interface using the gradient in reflectivity.

1224
1225
1226
1227
1228
1229
1230
1231
1232
1233
1234
1235
1236
1237
1238
1239
1240
1241
1242
1243
1244
1245
1246
1247
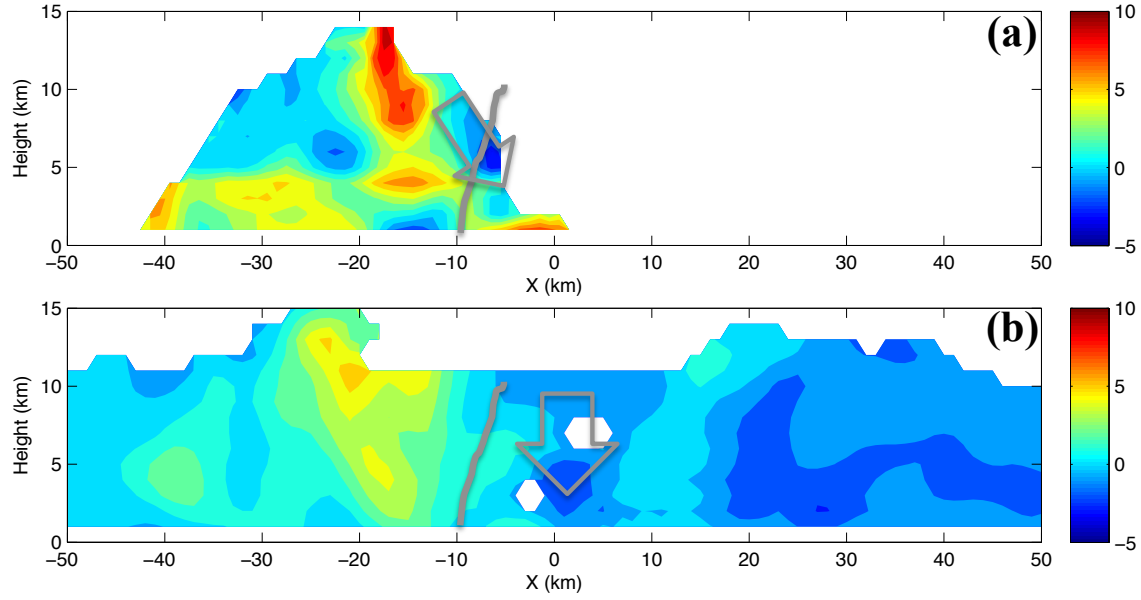
Figure 15. As in Fig. 13, only for vertical winds. The gray line denotes the western eye-eyewall interface using the gradient in reflectivity. The large gray arrows highlight features discussed in the text.

1257
1258
1259
1260
1261
1262
1263
1264
1265
1266
1267
1268
1269
1270
1271
1272
1273
1274
1275
1276
1277

1278
1279
1280
1281
1282
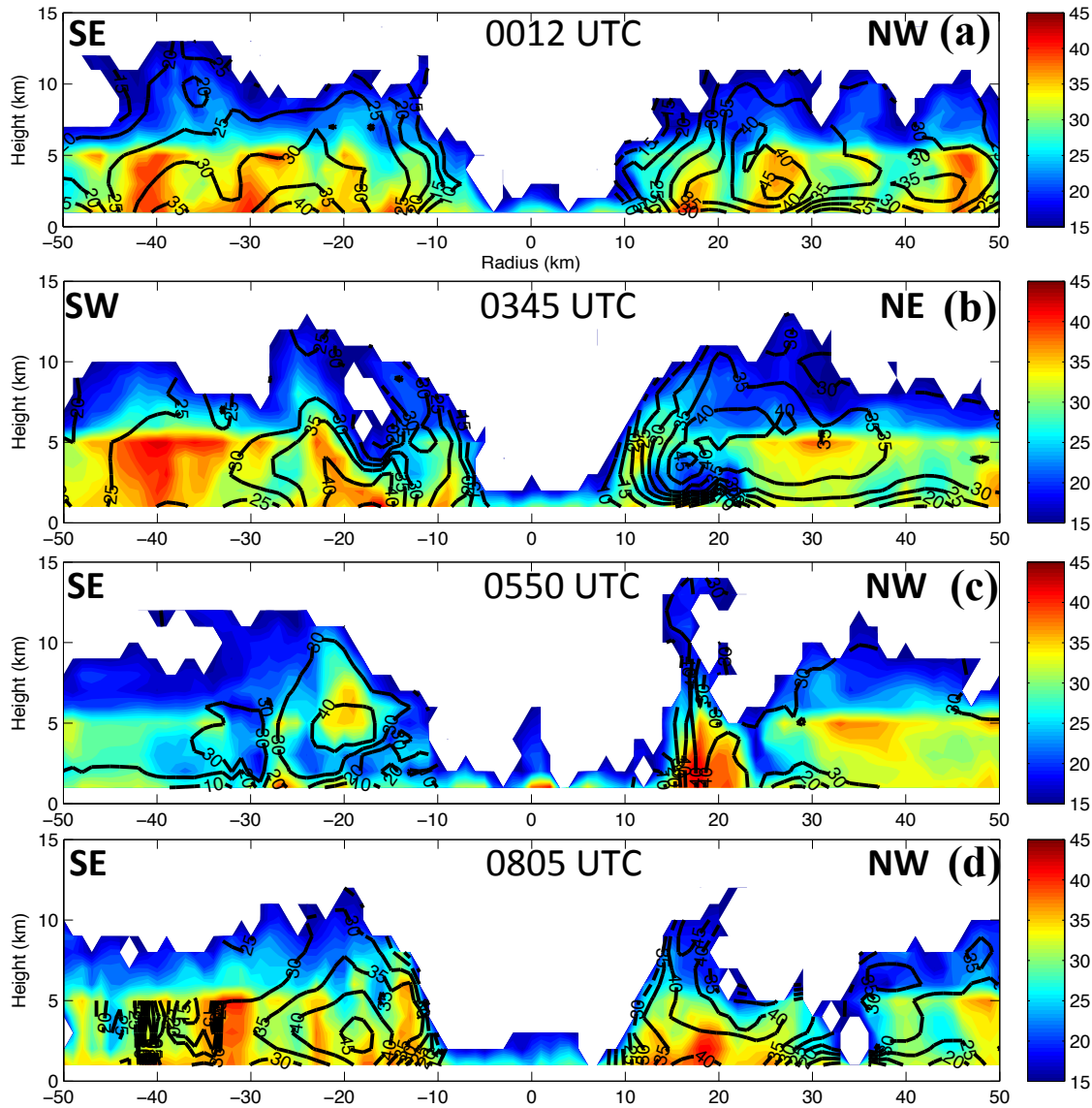
1283
1284
1285 Figure 16. HIWRAP vertical cross sections of Ku band reflectivity (shading; dBZ) and
1286 tangential winds (contours; m s^{-1}) at nadir for the Global Hawk overpasses on 17
1287 September centered at (a) 0012 UTC in southeast to northwest direction (b) 0345 UTC in
1288 southwest to northeast direction (c) 0550 UTC in southeast to northwest direction and (d)
1289 0805 UTC in southeast to northwest direction.
1290
1291
1292
1293
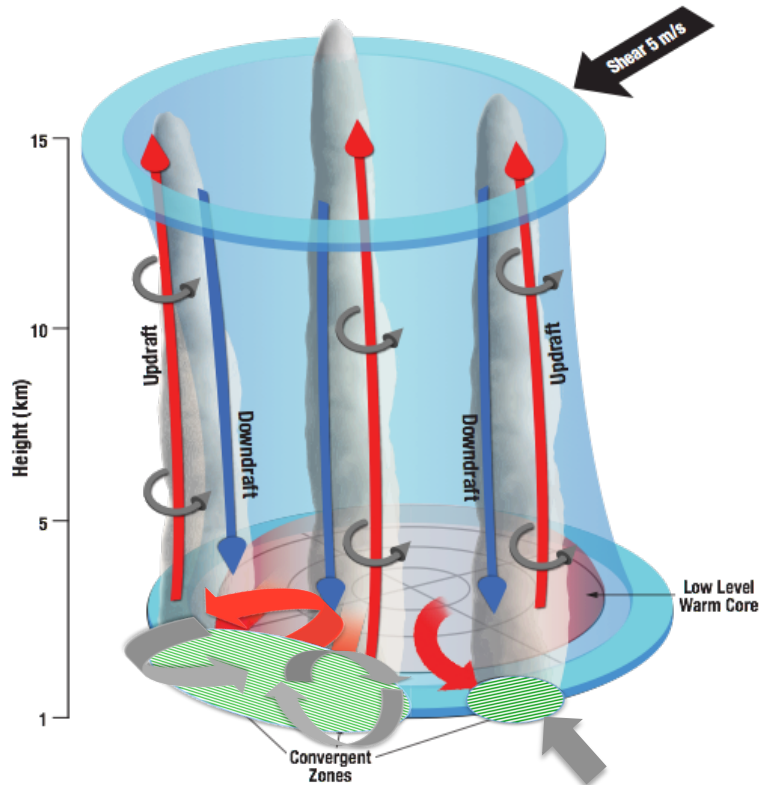
1294
1295
1296   Figure 17. Conceptual diagram highlighting the measurements and analysis from the
1297   HIWRAP, HAMSR and P3 instruments during the Hurricane Karl (2010) sampling. The
1298   arrows represent the mesoscale flow with red indicating anomalously warm, buoyant air.
1299
1300
1301
1302
1303
1304
1305
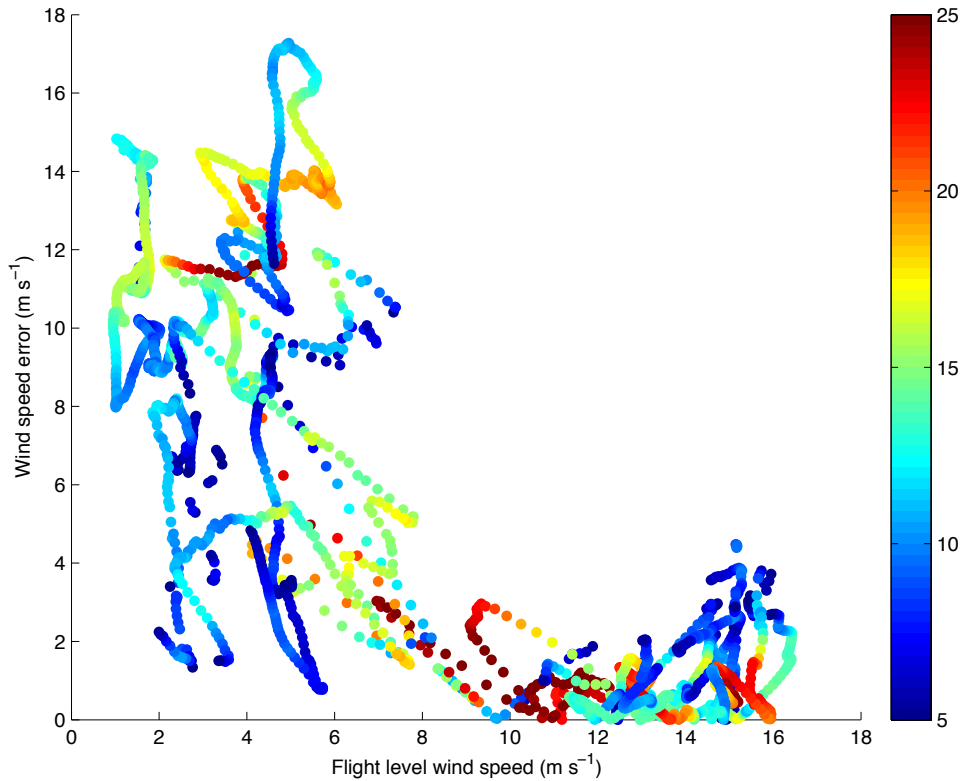
1306
1307
1308 Figure A1. Scatter plot of HIWRAP horizontal wind speed errors (|HIWRAP – P3 flight
1309 level|) vs. P3 flight level wind speeds for the coordinated flight during HS3 on 25 Sept.
1310 2013. The points are colored by HIWRAP Ku band reflectivity. Note the HIWRAP
1311 winds are computed using Ku band Doppler velocities. See text for more details.
1312
1313
1314
1315
1316
1317
1318
1319
1320
1321
1322
1323
1324
1325
1326
1327
1328
1329
1330
1331

1332
1333
1334
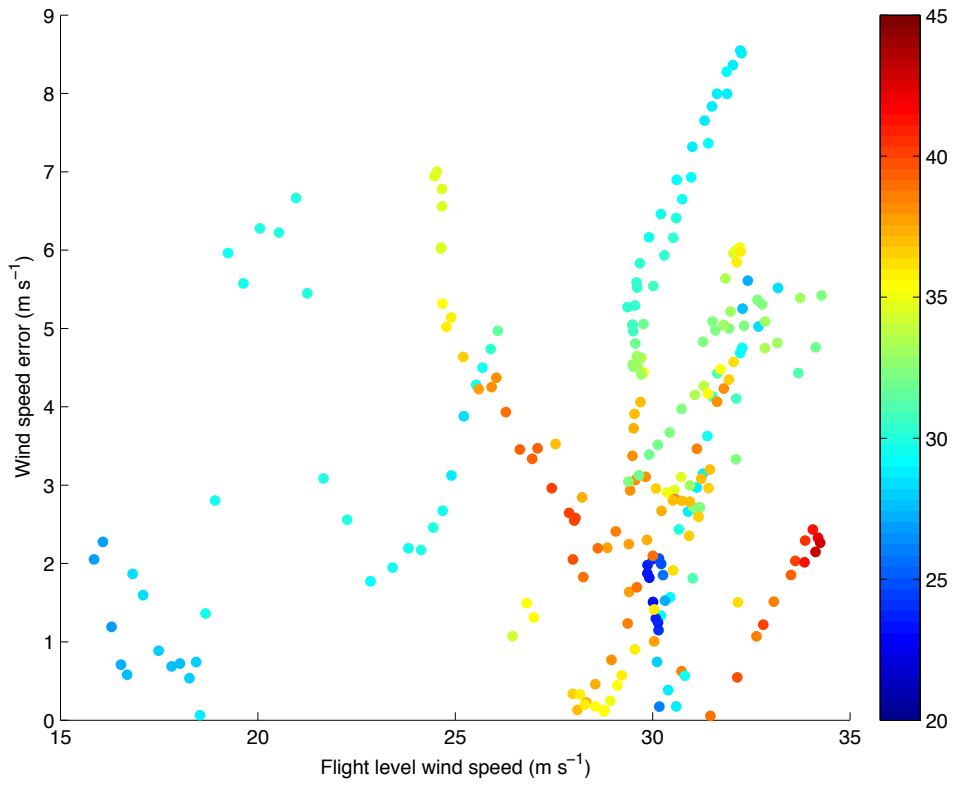
1335
1336
1337   Figure A2. As in Fig. A1, only for the coordinated flight during GRIP (sampling of
1338   Hurricane Karl on 16 Sept. 2010 at ~ 2040 UTC). The points are colored by HIWRAP
1339   Ku band reflectivity. Note the HIWRAP winds are computed using a combination of Ku
1340   and Ka band Doppler velocities. See text for more details.
1341